

Special Section:

The Arctic: An AGU Joint Special Collection

Key Points:

- Spatially explicit peat basal age, peat expansion, run-on and runoff are considered for a pan-Arctic Holocene simulation
- The estimated pan-Arctic peatlands soil C stock is 396–421 Pg C, and the Holocene average C accumulation rate was 22.9 g C·m⁻² yr⁻¹
- If current permafrost regions thaw, the peat C accumulation rate of the entire pan-Arctic region will likely decrease

Supporting Information:

Supporting Information may be found in the online version of this article.



Correspondence to:Q. Zhuang,
qzhuang@purdue.edu**Citation:**

Zhao, B., Zhuang, Q., & Frolking, S. (2022). Modeling carbon accumulation and permafrost dynamics of northern peatlands since the Holocene. *Journal of Geophysical Research: Biogeosciences*, 127, e2022JG007009. <https://doi.org/10.1029/2022JG007009>

Received 19 MAY 2022

Accepted 31 OCT 2022

Modeling Carbon Accumulation and Permafrost Dynamics of Northern Peatlands Since the Holocene

Bailu Zhao¹ , Qianlai Zhuang^{1,2} , and Steve Frolking³

¹Department of Earth, Atmospheric, and Planetary Sciences, Purdue University, West Lafayette, IN, USA, ²Department of Agronomy, Purdue University, West Lafayette, IN, USA, ³Institute for the Study of Earth, Oceans, and Space, University of New Hampshire, Durham, NH, USA

Abstract Northern peatlands are a large C stock and often act as a C sink, but are susceptible to climate warming. To understand the role of peatlands in the global carbon-climate feedback, it is necessary to accurately quantify their C stock changes and decomposition. In this study, a process-based model, the Peatland Terrestrial Ecosystem Model, is used to simulate pan-Arctic peatland C dynamics from 15 ka BP to 1990. To improve the accuracy of the simulation, spatially explicit water run-on and run-off processes were considered, four different pan-Arctic peatland extent data sets were used, and a spatially explicit peat basal date data set was developed using a neural network approach. The model was calibrated against 2055 peat thickness observations and the parameters were interpolated to the pan-Arctic region. Using the model, we estimate that, in 1990, the pan-Arctic peatlands soil C stock was 396–421 Pg C, and the Holocene average C accumulation rate was 22.9 g C·m⁻² yr⁻¹. Our estimated peat permafrost development history generally agrees with multi-proxy-based paleo-climate data sets and core-derived permafrost areal dynamics. Under Anthropocene warming, in the freeze-thaw and permafrost-free regions, the peat C accumulation rate decreased, but it increased in permafrost regions. Our study suggests that if current permafrost regions switch to permafrost-free conditions in a warming future, the peat C accumulation rate of the entire pan-Arctic region will decrease, but the sink and source activities of these peatlands are still uncertain.

Plain Language Summary In this study, we used a process-based model, the Peatland Terrestrial Ecosystem Model (PTEM), to simulate pan-Arctic peatland C dynamics from 15 ka BP to 1990. We revised PTEM 2.0 and considered spatially explicit peat initiation and peat expansion process in the simulation. The simulation shows that in 1990, part of the pan-Arctic peatlands soil C stock is 396–421 Pg C, and the Holocene average C accumulation rate was 22.9 g C·m⁻² yr⁻¹. These estimates have uncertainties in terms of peatland extent, peat expansion, and peat initiation processes. During the Little Ice Age cooling period and Anthropocene warming, part of the pan-Arctic region developed permafrost and thawed, other regions always had no permafrost. Under Anthropocene warming, in the freeze-thaw and permafrost-free regions, the peat C accumulation rate decreased, but it increased in permafrost regions. This result suggests if permafrost regions switch to permafrost-free conditions, the peat C accumulation rate of the entire pan-Arctic region will decrease with higher temperature.

1. Introduction

Northern peatlands (north of 45°N) comprise a soil C stock of 300–1,045 Pg C (Table 1). The Arctic region has been experiencing around three times the global average warming (Allen et al., 2018; GISTEMP-Team, 2021) which might increase regional peatland C release due to the acceleration of peat decomposition (Frolking et al., 2011; Gallego-Sala et al., 2018). In addition to the direct influence of temperature on decomposition, peatlands are also susceptible to indirect influences of climate change and anthropogenic activities. For example, peatland drainage lowers peatland water table and increases decomposition (Huang et al., 2021; Qiu et al., 2021) and peatland fires result in large carbon emissions (Turetsky et al., 2015).

Peatland C accumulation in permafrost-affected regions under a changing climate is influenced by permafrost dynamics. As permafrost thaws, C in newly thawed soil becomes susceptible to anaerobic and aerobic decomposition (O'Donnell et al., 2012; Turetsky et al., 2002). Permafrost thaw can also enhance soil C loss via the outflow of dissolved organic C (Hugelius et al., 2020; Plaza et al., 2019). Meanwhile, permafrost thaw also shifts the microbial community to one that benefits methane emissions (McCalley et al., 2014). Several studies have

© 2022. The Authors.

This is an open access article under the terms of the [Creative Commons Attribution License](https://creativecommons.org/licenses/by/4.0/), which permits use, distribution and reproduction in any medium, provided the original work is properly cited.

Table 1
Comparison Between Regional Peat C Stocks and CAR

Regional SOC stocks ^a (Pg C)	Source
397	This study (with Melton et al., 2022 peatland coverage)
421	This study (with Hugelius et al., 2020 peatland coverage)
396	This study (with Xu et al., 2018 peatland coverage)
404	This study (with average peatland coverage)
408	Qiu et al. (2019)
300	Hugelius et al. (2013) (Top soil 3m)
545–1,045	Nichols and Peteet (2019) with different estimation of CAR
400	Hugelius et al. (2020)
547	Yu et al. (2010)
436	Loisel et al. (2014)
365–550	Spahni et al. (2013) with different peatland extents
351	Müller and Joos (2021)
455	Gorham (1991)
Holocene CAR (g C·m ⁻² ·yr ⁻¹)	
22.9	This study
22.9 ± 2	Loisel et al. (2014)
18.6	Yu et al. (2009)
19.7–50.5	Nichols and Peteet (2019)
21.4	Chaudhary et al. (2020)
17.3–26.1	Turunen et al. (2002)
14.2–23.2	Treat, Jones, Camill, et al. (2016)

^a Regional SOC stocks refer to the pan-Arctic region.

modeled permafrost thaw and subsequent peatland C dynamics under climate warming, indicating that in sporadic and discontinuous permafrost peatlands, permafrost thaw will cause peatlands to be a weaker sink of 0.1 kg C·m⁻² or a source of up to 3 kg C·m⁻² in total during 2015–2100 from by 2100 (Jones et al., 2017; Treat, Jones, Alder, et al., 2021). While studies project the entire northern peatlands will possibly continue being C sinks until 2100, after which substantial C loss is projected as a result of permafrost thaw and decomposition increase (Chaudhary et al., 2017; McGuire et al., 2018). In contrast to the future projections, historical peatland permafrost changes during the Holocene and permafrost-C dynamics relationship are less studied. Although an existing study has established pan-Arctic permafrost aggradation and degradation history during the Holocene and found permafrost thaw in the past 300 yr, the history is reconstructed from sporadic core data and is limited in both its spatial and temporal coverage (Treat & Jones, 2018). Therefore, we intend to fill this knowledge gap by reconstructing continuous pan-Arctic permafrost dynamics during the Holocene.

In this study, a process-based model, the Peatland Terrestrial Ecosystem Model (PTEM), designed to simulate peatland ecosystem dynamics, is used. Although PTEM has been applied to various northern peatland sites and the simulated C accumulation processes is consistent with the core data (Zhao, Zhuang, Treat, & Frohling, 2022), simulating northern peatlands dynamics and permafrost conditions in the Holocene at the pan-Arctic scale with the existing version still has a couple of challenges. First is the current peatland extent is highly uncertain. A PTEM 1.0 simulation study used a fixed peatland area and uniform peat initiation age in the North America, resulting in considerable uncertainties in the estimation of present-day North America peatland C stock (Zhuang et al., 2020). After revision, PTEM 2.0 still does not simulate peatland spatial extent dynamics. Although multiple process-based models have simulated the dynamic peatland spatial extent with TOPMODEL, the uncertainty remains an issue (Qiu et al., 2019; Stocker et al., 2014). To quantify these uncertainties, three northern peatland coverage maps are selected (Hugelius et al., 2020; Melton et al., 2022; Xu

et al., 2018), and the soil C stock is estimated based on different observation-based data sets and the mean of these data sets, respectively.

Second, there is a limited number of observational records on peatland initiation time. Recently, Chaudhary et al. (2020) generated a spatial map of peatland basal initiation dates for the pan-Arctic region by interpolation from existing data sets of observed basal initiation dates (Gorham et al., 2007; Korhola et al., 2010; MacDonald et al., 2006). However, a limitation of spatial interpolation is that it emphasizes the effect of spatial autocorrelation on peat initiation, while ignoring the effect of local environment. To address this issue, we use a machine learning approach to estimate peat initiation year across the pan-Arctic based on data of temperature, precipitation, CO₂ concentration, latitude, longitude, and observed basal dates.

Third, there is information on peatland expansion at the regional scale, but no information on spatially explicit peat expansion (Gorham et al., 2007). We address this issue by establishing a spatially explicit pan-Arctic peatland expansion trend from existing data sets. Finally, the existing PTEM 2.0 is designed for site-level simulation. With no run-on and runoff considered, the variation of water and nutrient status (i.e., fen/bog status) were identified from exiting peat cores (Zhao, Zhuang, Treat, et al., 2022). There is no core information for most of the pan-Arctic region. We thus address this issue by developing a new version PTEM 2.1 considering grid-specific water run-on and run-off, and their impacts on peatland nutrient supply in PTEM 2.0 (Zhao, Zhuang, Treat, et al., 2022).

Built on the revised PTEM 2.1, this study analyzes peat C dynamics through the Holocene under different permafrost existence conditions in northern peatlands from initiation to 1990 (Appendix Figure S1 in Supporting Information S1). By doing so, this study answers the following questions: (a) what is the current northern peatland C

stock? (b) how has northern peatland permafrost changed during the Holocene? (c) how have northern peatland C dynamics changed historically? And (d) how have peatland C dynamics responded to historical climate change under different permafrost existence conditions? In this study, the historical peatland permafrost and C dynamics under climate variation are analyzed to help project the peatland response to more severe climate changes in the future.

2. Methods

2.1. Peatland Model Overview

PTEM simulates peatland dynamics at a $0.5^\circ \times 0.5^\circ$ resolution. In a previous work (Zhao, Zhuang, Treat, et al., 2022), PTEM 1.0 was revised to improve the representation of biogeochemical processes of peatlands. In particular, PTEM 2.0 models the vegetation C and N pools considering three plant functional types (PFTs): moss, herb, and shrub/small trees. The monthly C assimilated by vegetation is distributed to each PFT by their relative dominance. The dominance of vascular plants are influenced by WTD, shrubs/small trees prefers deeper WTD than moss, and herb prefers the shallowest WTD. Meanwhile, the thriving of vascular plants has a negative effect on the growth of moss due to shadowing effect. The peatland NPP is the sum of NPP from three PFTs. The NPP of each PFT is simulated based on its vegetation C, the demand for N and the peatland N availability. The amount of N available to vegetation originates from net N mineralization, by converting organic N into inorganic form. The organic N originates from the litter N from the three PFTs. Monthly total litter C from the three PFTs is the monthly litter C input. As litter C from different PFTs will have various decomposition rates, the mean decomposition rate of the monthly peat litter input is the average of three decomposition rates, weighted by the fraction of monthly litter C amount from each PFT. The peat is divided into 1 cm layers from peat bottom to the top, while the top layer can be thinner than 1 cm. In each month, new litter C is added to the top layer and peat in all layers decomposes. This process usually makes the top layer thicker and the other layers thinner. Thereafter, the layer thicknesses from the bottom to the top are added to get the new peat thickness. Next, the peat is re-interpolated into 1 cm layers and the soil bulk density, soil C content, fraction of remaining original litter and decomposition rate are re-calculated for each layer. By interpolation, each 1 cm peat layer is composed of litter from multiple continuous months and usually years, while the layer age is not tracked. The total peat thickness can be estimated from the number of 1 cm layers and the thickness of the top layer. And the total soil C stock on unit area can be estimated by adding the soil C content in each layer. N pool is not divided into layers and is not influenced by the interpolation process.

Decomposition in PTEM 2.0 includes aerobic and anaerobic decomposition. Aerobic decomposition mainly occurs above the water table and is influenced by that layer's temperature and moisture. Given the soil C amount, litter, aerobic decomposition rate increases exponentially with temperature. Above the water table, aerobic decomposition increases with soil moisture until soil moisture reaches a threshold, then aerobic decomposition starts decreasing with soil moisture (Zhao, Zhuang, Treat, et al., 2022, Equations S13–S14 in Supporting Information S1). The temperature in each 1 cm peat layer is interpolated from the soil thermal profile derived from soil thermal module (STM). Compared with the PTEM 1.0 in Zhuang et al. (2020), PTEM 2.0 has an improved initialization process of STM which more accurately simulates the active layer thickness (ALT) dynamics at the site level (Zhao, Zhuang, Treat, et al., 2022). After initialization, STM calculates monthly soil temperature in a 25-layer profile with the initial deepest layer 43.5 m below surface (Zhuang et al., 2001). PTEM 2.0 assumes the top layer is a 10 cm moss layer, followed by a soil organic layer. As peat accumulates, the depth of the soil organic layer and the total simulation depth of STM changes. The depth and soil water content of the organic layer in STM are updated monthly, thereby influencing the soil thermal properties in this layer.

Soil moisture is calculated by a monthly hydrology module. PTEM 2.0 divides the soil profile into three hydrological layers: moss, organic and mineral. Water flows vertically from upper to lower layers, and soil moisture in each layer is calculated. Water table depth is calculated by the algorithms in Granberg et al. (1999), which is a function of volumetric moisture in the moss (10 cm in this study) and the organic layer above the maximum WTD (25 cm in this study). Below the water table, decomposition is dominated by anaerobic processes and the decomposition rate is influenced by temperature and soil pH. Similar to aerobic decomposition, anaerobic decomposition rate increases exponentially with temperature (Zhuang et al., 2004). In PTEM 2.0, we assume that, when the soil is acidic, the methane production rate increases with pH values. Soil pH declines gradually from 6.5 to 4.2 as fens transition to bogs, and the decrease in methane production is usually simultaneous (Zhao, Zhuang,

Treat, et al., 2022). The PTEM 2.0 fen-bog transition at the site-level happens when peat thickness exceeds a certain threshold determined by peat core profiles. As fens shift to bogs, the maximum C assimilation rate of peatlands and litter C decomposition rate of each PFT will decrease by certain fractions, which were calibrated from peat core profiles (Zhao, Zhuang, Treat, et al., 2022, Equations S21–S22 in Supporting Information S1). At the pan-Arctic level, we assume fen-to-bog transition happens as water run-on declines, leading to lower soil pH (Section 2.2). Notably, although both aerobic and anaerobic decomposition are simulated, the anaerobic decomposition rate is generally lower than the aerobic decomposition rate. In addition, PTEM 2.1 assumes no decomposition in the frozen soil layer.

2.2. Water Run-On and Run-Off

Water run-off is modeled with the physical equation proposed by Weiss et al. (2006):

$$R_{off} = -\frac{T_r w \left(\frac{dh}{dl}\right)}{A} \times m_{day} \times 1,000 \quad (1)$$

where R_{off} is run-off ($\text{mm}\cdot\text{mon}^{-1}$), T_r is transmissivity ($\text{m}^2\cdot\text{d}^{-1}$), w is the vertical width of the hydrological active layer (m) within which WTD fluctuates, dh/dl is the local slope of the water table, A is the unit horizontal area and m_{day} is the number of days within a month (Appendix Table S1 in Supporting Information S1). Transmissivity (T_r) is given by:

$$T_r = a_t e^{(-b_t z_{wt})} \quad (2)$$

where a_t ($\text{m}^2\cdot\text{d}^{-1}$) and b_t (m^{-1}) are parameters given by Granberg et al. (1999), z_{wt} is WTD (m, negative values down from the peat surface).

The GMTED 2010 global 1 km resolution DEM data (USGS & NGA, 2010) and 1 km resolution monthly WTD products (Fan et al., 2013) were used to derive the local water table slope. The Fan et al. (2013) data set was selected because it is based on numerous observations and gives a reasonable estimation of Alaska and Canada wetland areas. Notably, this data set does not consider any impact of water pumping or drainage on WTD (Fan et al., 2013). For each $0.5^\circ \times 0.5^\circ$ grid, the 1×1 km grid cells with WTD shallower than 0.25 m were picked as wetland grid cells. In particular, for each of these 1×1 km wetland grid cells, the local slope of the water table (dh/dl) in eight directions (corresponding to eight neighboring grid cells) were calculated. Since water table slope is defined as dh/dl along the direction of maximum water head decrease (Cheremisinoff, 1997), the maximum value is picked as the local water table slope. In particular, dl is 1 km or $\sqrt{2}$ km depending on the relative location of the two grid cells. dh is the spatially explicit difference between WTD in two grid cells:

$$dh = (H_1 + z_{wt1}) - (H_2 + z_{wt2}) \quad (3)$$

where H_1 and H_2 are the elevation of two adjacent grid cells (m), z_{wt1} and z_{wt2} are the WTD of two adjacent grid cells (m, negative values suggest below surface), with grid cells indices specified so that dh is always positive. The local water table slope of all 1×1 km grid cells within a $0.5^\circ \times 0.5^\circ$ grid were averaged to get that grid cell's mean wetland water table slope. Twelve monthly local water table slopes were calculated for each $0.5^\circ \times 0.5^\circ$ grid corresponding to 12 months in the WTD product, and the annual average was used in the long-term simulation. The annual average value is used because the seasonal variation for wetland water table slope is not obvious (Appendix Figure S20 in Supporting Information S1). This grid-specific wetland mean annual water table slope is assumed as constant throughout the simulation.

The algorithm for calculating run-on was adopted and simplified from the Holocene Peatland Model (Frolking et al., 2010), which assumes run-on declines with peat thickness in a sigmoid function:

$$R_{on} = \frac{Ron_{max}}{1 + \exp(a_r \times z_{peat} + b_r)} \quad (4)$$

where R_{on} is run-on ($\text{mm}\cdot\text{mon}^{-1}$), Ron_{max} is the maximum run-on of each $0.5^\circ \times 0.5^\circ$ grid, a_r (cm^{-1}) and b_r are fitting parameters and z_{peat} is peat thickness (cm). Ron_{max} was estimated by the maximum run-off from eight

surrounding $0.5^\circ \times 0.5^\circ$ grid cells calculated by Equation 1, and is a constant for each grid cell. The method of deriving the parameters in Equation 4 is given in Appendix Text S1 in Supporting Information S1.

The amount of dissolved nitrogen entering the peat is:

$$N_{water} = R_{on\ mon} \times N_{cont\ ground} + P_{through\ mon} \times N_{cont\ rain} \quad (5)$$

where N_{water} is the monthly nitrogen brought into peat water via run-on and precipitation ($\text{g} \cdot \text{mon}^{-1}$), $R_{on\ mon}$ is the monthly run-on ($\text{mm} \cdot \text{mon}^{-1}$), $N_{cont\ ground}$ is the nitrogen concentration in ground water ($\text{g} \cdot \text{mm}^{-1}$), $P_{through\ mon}$ is the monthly precipitation that travels through the canopy and arrives at the ground ($\text{mm} \cdot \text{mon}^{-1}$), and $N_{cont\ rain}$ is the nitrogen concentration in rain water ($\text{g} \cdot \text{mm}^{-1}$) (Appendix Table S1 in Supporting Information S1). In addition, peatland pH is assumed to decrease simultaneously as run-on declines, and the trend is derived from Equation 4:

$$pH = pH_{min} + \frac{pH_{max} - pH_{min}}{1 + \exp(a_r \times z_{peat} + b_r)} \quad (6)$$

where pH_{min} and pH_{max} are the minimum and maximum pH of peatlands (Appendix Table S1 in Supporting Information S1), a_r , z_{peat} and b_r are the same as in Equation 4.

2.3. Peat Initiation

To estimate the basal dates of the grid cells without available records, a neural network (NN) approach was used (Pedregosa et al., 2011). First, the training data were obtained and processed. Peat basal date data in Loisel et al. (2017), Treat, Jones, Brosius, et al. (2016), Treat, Jones, Camill, et al. (2016), and Yu et al. (2010) were used, selecting only dates with site latitude $\geq 45^\circ\text{N}$ and basal date ≤ 15 ka BP ($n = 8,590$). These points were grouped into $0.5^\circ \times 0.5^\circ$ grid cells and the oldest basal date in each grid cell was selected ($n = 1,643$; Figure 2a). Independent variables selected to train the NN model included mean annual temperature ($^\circ\text{C}$), precipitation ($\text{mm} \cdot \text{day}^{-1}$), CO_2 concentration (ppm), latitude and longitude, and peat existence (0/1) was the dependent variable. Temperature, precipitation and CO_2 concentration were chosen because they directly influence plant productivity and litter decomposition. Latitude and longitude were chosen because peat plant establishment is related to plant propagule migration from nearby grid cells and is likely to show spatial-autocorrelation (Gorham et al., 2007). The temperature, precipitation and CO_2 concentration data originate from the decadal TraCE 21 ka data set (He, 2011) and were interpolated to $0.5^\circ \times 0.5^\circ$ grid cells. For each grid cell, a set of input data consisted of five independent variables and one dependent variable was generated for each decade from 15 ka BP to 1990. This resulted in 1,504 sets of samples for each grid cell and 2,471,072 ($=1,504 * 1,643$) sets for all grid cells. With 80% of these sets of samples used as training data sets and the rest as testing data sets the ~ 2 million sets of training samples were likely to be sufficient to train the model.

The second step was to train a multi-layer perceptron (NN) model. There were three hidden layers with 16, 64, and 10 nodes in each layer, respectively. In addition, an activation layer was added and the hyperbolic tangent function was selected as the activation function. Eighty percent of these input data were randomly chosen to train the model and the rest were testing samples.

Third, the NN model was applied to the grid cells without basal records and basal dates were calculated from the NN model outputs. For each grid cell, the model outputs were a time series (10 yr time step) of 0s and 1s, and the peat basal date was defined as the time when outputs switch from 0-dominated to 1-dominated. In order to find this transition, the time series was fitted by Matlab fitglm function and two fitting coefficients were derived for each grid cell (Appendix Figure S3 in Supporting Information S1). In cases in which the calculated basal dates were older than 15 ka BP or younger than 1990 (425/24,903 grid cells, 1.7%), an alternative algorithm was used. Assume i is the decade number between 15 ka BP and peat initiation, $(1,504-i)$ is the decade number between peat initiation and 1990, n_{pos} is the number of 1s in the output time series, $p11$ is the precision score of the model (i.e., the ratio between the true positive number and the total predicted positive number), and $p01$ is one minus

$p11$ (i.e., the ratio between the false positive number and the total predicted positive number), then $n\ pos$ can be calculated as:

$$n\ pos = i \times p01 + (1,504 - i) \times p11$$

$$\text{so } i = \frac{n\ pos - p11 \times 1504}{p01 - p11} \quad (7)$$

Where $p01$ and $p11$ are both derived from testing the trained model against the testing data set. Finally, the basal date (yr BP) corresponding to decade i is:

$$\text{basal} = (1500 - i) \times 10 \quad (8)$$

2.4. Peat Expansion in a Grid Cell

PTEM 2.0 does not simulate peatland areal shrinkage and expansion within a simulation grid, and spatially explicit peat expansion in this study originated from downscaling a pan-Arctic peatland expansion trend. A similar method has been used in Nichols and Peteet (2019). At the pan-Arctic scale, the cumulative distribution function (CDF_{reg}) of peat basal age of $0.5^\circ \times 0.5^\circ$ grid cells was fitted to a logistic function (Figure 1d):

$$\text{CDF}_{reg}(\text{basal}) = \frac{1}{1 + \exp[a_c \times (15,000 - \text{basal}) + b_c]} \quad (9)$$

where a_c and b_c are fitting parameters, and basal is the peat basal date in year BP. This CDF describes the trend of peat expansion at the regional scale, and we assumed that the same trend is applicable to the peat expansion in each single grid cell since initiation (Appendix Figure S5a in Supporting Information S1):

$$\begin{cases} f_{peat}(yr) = 0 & yr < \text{basal} \\ f_{peat}(yr) = \frac{1}{1 + \exp[a_c \times (15000 - yr) + b_c]} & yr \geq \text{basal} \end{cases} \quad (10)$$

where f_{peat} is the ratio between peat coverage in yr (year) compared with the current peat coverage, and yr is the simulation year in BP. Therefore, if the peatland coverage in a given grid cell is $n\%$, the peatland fraction in a given year is $n\% \times f_{peat}(yr)$.

2.5. Pan-Arctic Calibration

For a regional simulation, calibrating a model with a few sites and applying the parameters to the whole region can cause considerable uncertainties, especially for a 15 ka simulation. The estimation of run-on is also likely to introduce uncertainties due to the dependence on other model-based data sets (i.e., Fan et al., 2013; Hugelius et al., 2020) and the hypothetical run-on and peat thickness relationship. To reduce these uncertainties, we calibrated PTEM 2.1 with numerous peat thickness records and interpolated the parameters to the pan-Arctic region using the Kriging method in ArcMAP 10.7. In particular, the peat thickness records were obtained from Hugelius et al. (2020), Loisel et al. (2014), Treat, Jones, Camill, et al. (2016) ($n = 7,812$). These records were grouped into $0.5^\circ \times 0.5^\circ$ grid cells and the thickest peat record in each grid cell was selected for calibration ($n = 2,055$). Peat thickness was chosen for calibration because it has the most records and can approximately represent the peat soil C. A previous study simulating peat C accumulation with PTEM 2.1 at the site level (Zhao, Zhuang, Treat, et al., 2022) indicates that there are four important parameters for peat C accumulation: maximum C assimilated by the ecosystem (C_{max}) and heterotrophic respiration (R_H) at 0°C for the three PFTs (k_d for moss, herb and shrub/small trees, respectively). However, with only one peat thickness data value in each grid cell, it's not reasonable to calibrate four parameters. Therefore, the k_d values were calibrated against the flux tower-based ecosystem respiration at the Zackenberg, Greenland fen site for 2008–2016 (López-Blanco et al., 2020; Appendix Figure S4 in Supporting Information S1) and applied to the whole region, while the C_{max} values were calibrated for the 2055 grid cells and then spatially interpolated. The calibration was conducted with Model-Independent Param-

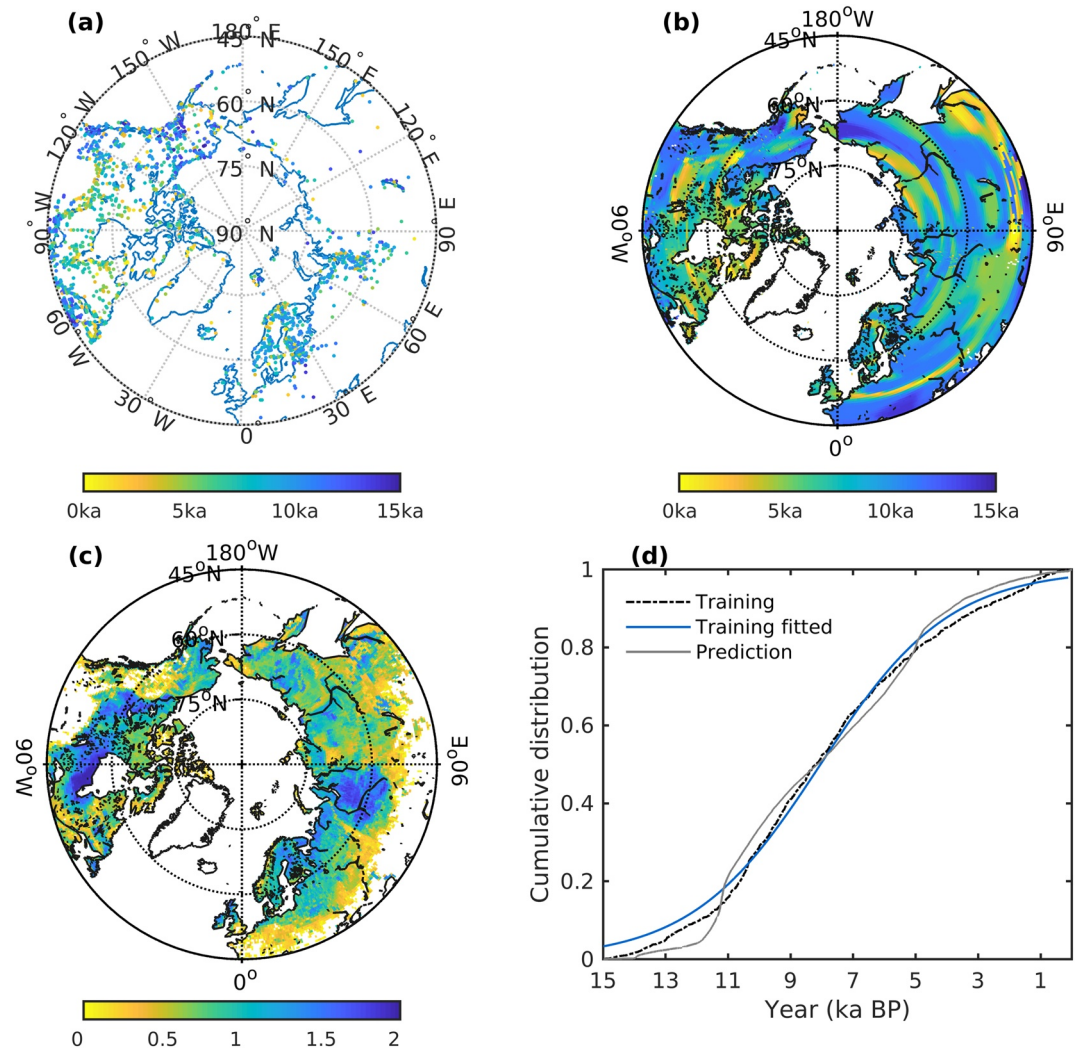


Figure 1. (a) Training basal dates of pan-Arctic peatlands (units: year BP); (b) the training and predicted basal dates of pan-Arctic peatlands (units: year BP); (c) log₁₀ of the average peatland coverage percent, where grid cells with <1% peatland coverage are left blank; (d) cumulative distribution function (CDF) (0–1) of the training and predicted basal date data set and the fitted line of the training CDF.

eter Estimation (PEST, v17.2 for Linux; Doherty et al., 2022.) and the correlation coefficient (R^2) between the observed and calibrated peat thickness is 0.94 (Figure 2).

2.6. Preliminary Model Simulations of Spatially Explicit Peat Depth-Area Fraction Relationship

In PTEM 2.1, peat is assumed to be a column of unit area which is vertically divided into 1 cm layers, and the soil C, CO₂, and CH₄ production are calculated for each layer. However, when considering peat expansion, the peat vertical profile is no longer a rectangle, but an irregular shape described by peat thickness and area relationship (Appendix Figure S5d in Supporting Information S1). Therefore, for a given month, the total soil C, CO₂, and CH₄ production are:

$$SOC_{tot} = \sum_{i=1}^n SOC_i \times f_{peat\ i} \quad (11)$$

$$CO_{2\ tot} = \sum_{i=1}^n CO_{2\ i} \times f_{peat\ i} \quad (12)$$

$$CH_{4\ tot} = \sum_{i=1}^n CH_{4\ i} \times f_{peat\ i} \quad (13)$$

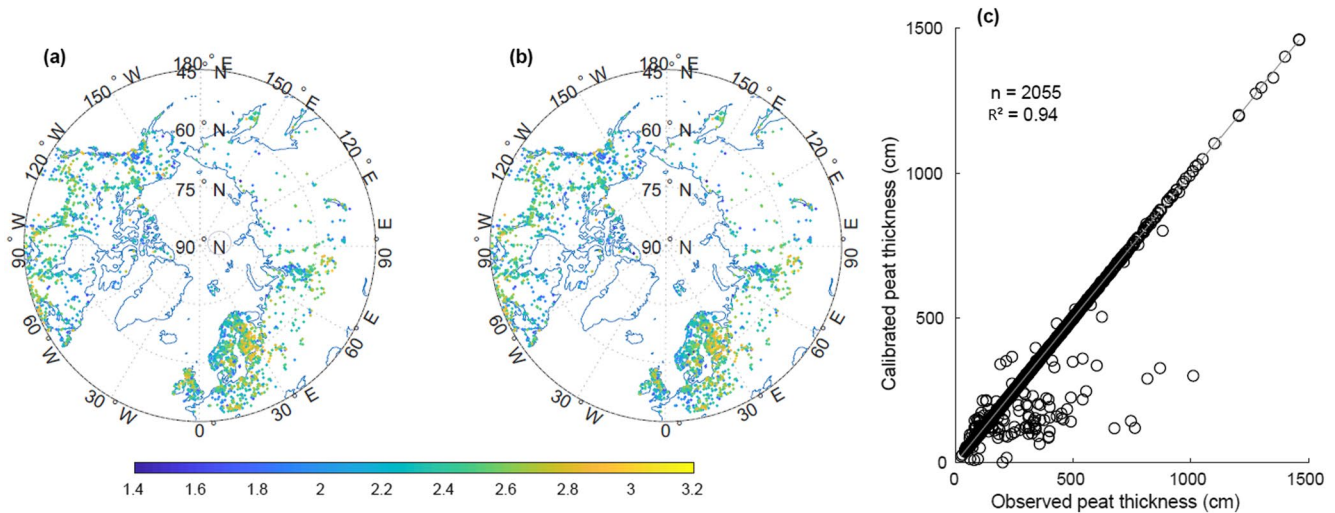


Figure 2. (a) Location and the \log_{10} of observed peat thickness ($\log_{10}(\text{cm})$) of the 2055 data points used for regional calibration. (b) Location and the \log_{10} of calibrated peat thickness ($\log_{10}(\text{cm})$) of the same 2055 data points. (c) Comparison between the observed peat thickness and calibrated peat thickness. The solid gray line is the 1:1 line.

where SOC_{tot} , $\text{CO}_{2\text{tot}}$, and $\text{CH}_{4\text{tot}}$ are the total soil C ($\text{g C}\cdot\text{m}^{-2}$), CO_2 emission ($\text{g C}\cdot\text{m}^{-2}\text{mon}^{-1}$) and CH_4 production ($\text{g C}\cdot\text{m}^{-2}\text{mon}^{-1}$), SOC_i , CO_{2i} , and CH_{4i} are the soil C, CO_2 emission, and CH_4 production in layer i , n is the number of layers and $f_{\text{peat } i}$ is the ratio between peat coverage in layer i compared with the final peat coverage at the top layer (Appendix Figure S5d in Supporting Information S1). As a result, it is necessary to get the $f_{\text{peat } i}$ for each layer i . In order to get this information, a preliminary PTEM 2.1 run was conducted to map the relationships between peat thickness and time, which was used to find the time when peat thickness first exceeds i cm (yr_i) (Appendix Figures S5b and S5c in Supporting Information S1):

$$\begin{aligned} \text{thick}_i &= h(\text{yr}_i) \\ \text{yr}_i &= h^{-1}(\text{thick}_i) \end{aligned} \quad (14)$$

where thick_i is integer peat thickness, i is the index of the 1 cm peat layer corresponding to thick_i . For each given layer i and thick_i , $f_{\text{peat } i}$ was calculated by substituting yr_i into Equation 10 (Appendix Figure S5d in Supporting Information S1). Afterward, a second PTEM 2.1 run was conducted with total soil C, CO_2 emission and CH_4 production calculated as Equations 11–13.

2.7. Model Input Data and Simulation Analysis

PTEM 2.1 requires monthly temperature ($^{\circ}\text{C}$), precipitation ($\text{mm}\cdot\text{mon}^{-1}$), cloudiness (0–1), and vapor pressure (hPa) as climate inputs. For the short-term WTD simulation, the climate data was derived from CRU v4.03 (CRU, 2018). For the Holocene simulation, the climate inputs were derived from monthly TraCE 21 ka data set (He, 2011). In particular, vapor pressure data were calculated from TraCE 21 ka relative humidity and temperature, and all four climate inputs were bias-corrected by CRU v4.03 data (Zhao, Zhuang, Treat, et al., 2022). In addition, PTEM 2.1 requires atmospheric CO_2 as an input, which was derived from the TraCE 21 ka data set. The other inputs include spatially explicit soil texture (FAO/UNESCO, 1974) and elevation (Zhuang et al., 2002).

Uncertainties in the peatland C stock partially arise from uncertainties in peatland coverage. Since PTEM 2.1 does not simulate peatland coverage, we use three different maps covering the pan-Arctic region (Hugelius et al., 2020; Melton et al., 2022; Xu et al., 2018). All maps were aggregated into $0.5^{\circ} \times 0.5^{\circ}$ grid cells with spatially explicit peatland abundance, and their average was used as a fourth map. The simulated results were mapped over different peatland extents to get a range of regional soil C and soil C decomposition.

2.8. Simulation Analysis

One research objective is to analyze the historical permafrost dynamics of northern peatlands. Permafrost existence in soil is defined as at least two continuous years with partially frozen soil. Notably, permafrost existence in peat is derived from comparing peat thickness and ALT. In particular, if ALT is thinner than peat thickness, then permafrost exists in peats, and vice versa. Therefore, permafrost existence in peat is different from permafrost existence in soil. When analyzing C dynamics, the average C accumulation rate (CAR) during a given time period is calculated as:

$$\text{CAR} = \frac{\Delta \text{soil organic C}}{\Delta t} \quad (15)$$

where $\Delta \text{soil organic C}$ is the difference in soil organic C ($\text{g C} \cdot \text{m}^{-2} \text{yr}^{-1}$) and Δt is the length of the period in years. In particular, Holocene CAR is calculated as ratio of the final soil organic C amount in 1990 and the number of years between peat initiation and 1990. PTEM 2.1 simulates the rates of aerobic and anaerobic decomposition, which emits CO_2 and CH_4 respectively. When analyzing, CO_2 emission and CH_4 production are added up as decomposition. Since CH_4 oxidation is not simulated, we do not use CH_4 production to represent CH_4 emission and thereby net greenhouse gas emissions are not analyzed.

The peatland C dynamics under past climate change is analyzed during 500a BP-1990, when the switch from cooling to warming climate leads to the changes in permafrost condition and C fluxes in the pan-Arctic region.

3. Results

3.1. Estimates of Regional Peat Basal Dates

We use 24,901 grid cells in the region for model simulation, 23,478 of them have predicted basal dates. In Eurasia, with insufficient training data, the predicted basal dates show unrealistic latitudinal patterns (Figure 1b). A possible reason is that the training data set does not well represent the whole Eurasia, which is indicated by the histogram of the input variables, which shows lacking samples in the Eastern hemisphere (Appendix Figure S5 in Supporting Information S1). However, most of these patterns are located in the region with low peatland coverage, and so should have limited influence on our regional simulation results (Figure 1c). When applying the model to the testing data sets, the accuracy of the NN model is 0.88, and F_1 score is 0.89, precision score and recall score are 0.87 and 0.90, respectively, indicating the model predicted peat existence with relatively high accuracy. The accuracy of the model is slightly improved by ~ 0.005 when the model is trained without precipitation, possibly due to the lack of representativeness in the training precipitation data (Appendix Figure S6 and Table S2 in Supporting Information S1). However, removing temperature, CO_2 concentration, latitude and longitude all results in slightly lower model accuracy, indicating the variables used to train the model are not independent and removing one or two does not influence the model accuracy significantly. With all combinations of model training variables in Appendix Table S2 in Supporting Information S1, when applying the model with training data sets, the model accuracy, precision score and recall score are the same as applying to the testing data sets. Therefore, no over-fitting was detected in the models. The correlation coefficient (R^2) between the CDF of the training and predicted data sets is 0.99 (Figure 1d). The CDF suggests that most of the peat was initiated during 11–4 ka BP.

3.2. Regional Soil C Stocks and C Fluxes

The simulated C accumulation rate (CAR) is first compared with other estimates from the literature (Loisel et al., 2014; Nichols & Peteet, 2019). The CAR is $22.9 \text{ g C} \cdot \text{m}^{-2} \text{yr}^{-1}$ during 15 ka BP-1990. The 500 yr bin CAR generally declined from 10 ka BP ($30.0 \text{ g C} \cdot \text{m}^{-2} \text{yr}^{-1}$) to present ($16.8 \text{ g C} \cdot \text{m}^{-2} \text{yr}^{-1}$; Figure 3a). This trend agrees with the core-derived data in Loisel et al. (2014) until 1.5 ka BP, when the cores suggest increasing CAR during 1.5 ka BP to present (Figure 3a). The correlation coefficient (R^2) of long-term core-derived CAR and the simulation-derived CAR is 0.25 (Figure 3b). In addition, our simulated trend agrees with the trend in Nichols and Peteet (2019) estimated from the lowest CAR, although our estimates are lower between 8 and 6 ka BP and higher after 5 ka BP (Figure 3a).

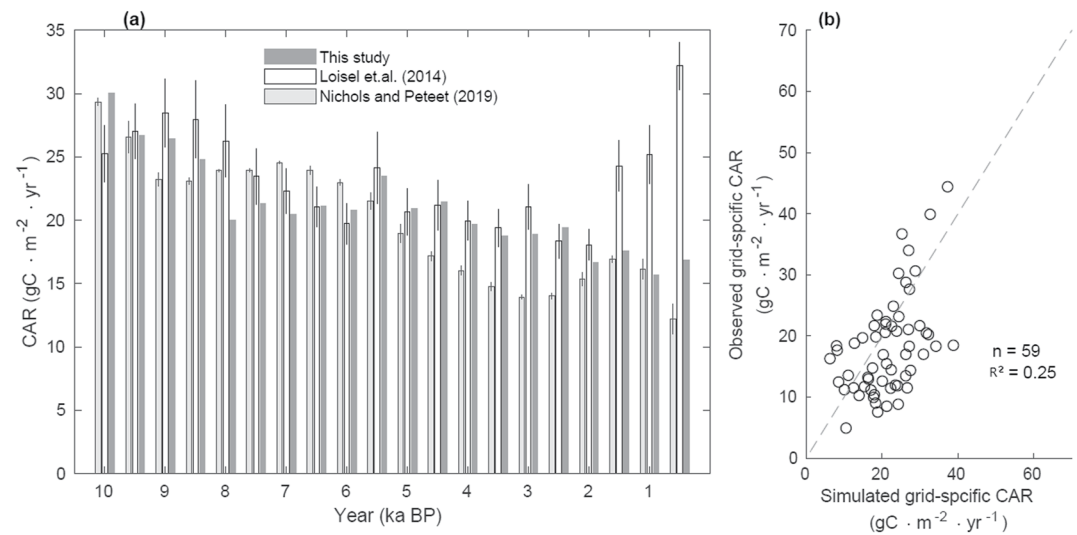


Figure 3. (a) Comparison of long-term C accumulation rate (CAR) from this study and the literature from 10 ka BP to present in 500 yr bins. The error bars are the standard deviation. (b) Comparison between the long-term core-derived CAR (Loisel et al., 2014) and simulated CAR in corresponding $0.5^\circ \times 0.5^\circ$ grid cells. The dash line is the 1:1 line.

The contemporary (i.e., 1990) peatland C stock is 396–421 Pg C depending on the peatland coverage maps, with 404 Pg C corresponding to the average coverage (Table 1). Although peat C started accumulation since 15 ka BP, no significant increase is found until 11–12 ka BP (Figure 4a), when peat C accumulation, CO_2 and CH_4 emissions increase simultaneously. In 1950 (0 ka BP), with average peatland coverage, the smoothed annual total decomposition is 303.9 Tg $\text{C} \cdot \text{yr}^{-1}$ (Figure 4b).

3.3. Regional Permafrost States in Peatlands

In order to evaluate the accuracy of PTEM 2.1 in simulating ALD and permafrost in peatlands, the model results are compared with multiple data sets (Brown et al., 2000; Hugelius et al., 2020; Obu et al., 2020; Treat, Jones, Camill, et al., 2016; Yi & Kimball, 2020). In particular, the simulated ALD in 1990 correlates better with satellite-derived Arctic ALD in 1997 (Obu et al., 2020) and satellite-derived Alaskan ALD in 2001 (Yi & Kimball, 2020; $R^2 = 0.66$ and 0.33 , respectively) than with the circumpolar observation network data from (Brown et al., 2000; $R^2 = 0.14$, Figures 5a–5c). When comparing the simulated permafrost existence in peat in 1990 with the core record (Hugelius et al., 2020; Treat, Jones, Camill, et al., 2016), the accuracy is 0.75 ($n = 1,504$, Figure 5d). In particular, accuracy is the fraction of grid cells that the simulated permafrost existence condition matches the core record. Overall, PTEM 2.1 captures permafrost existence/absence in peat, especially in continuous permafrost and non-permafrost regions.

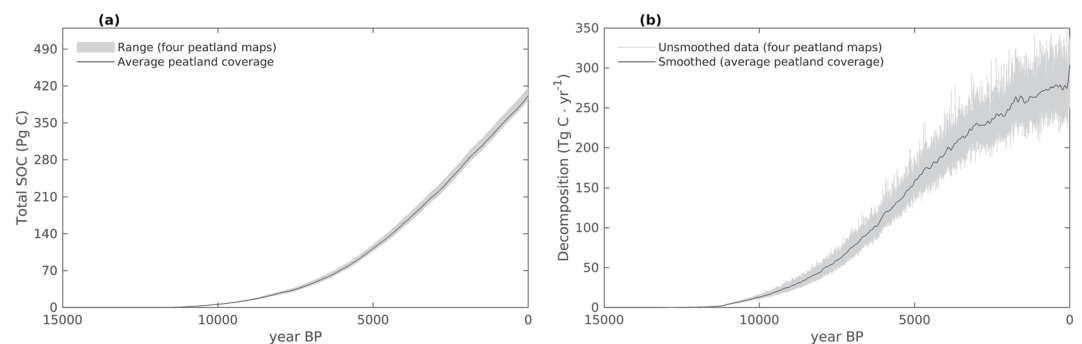


Figure 4. Time series of (a) pan-Arctic peatland C stocks; (b) pan-Arctic peatland C emissions from decomposition. The emissions of average peatland coverage in panel (b) are smoothed with Matlab's lowess function.

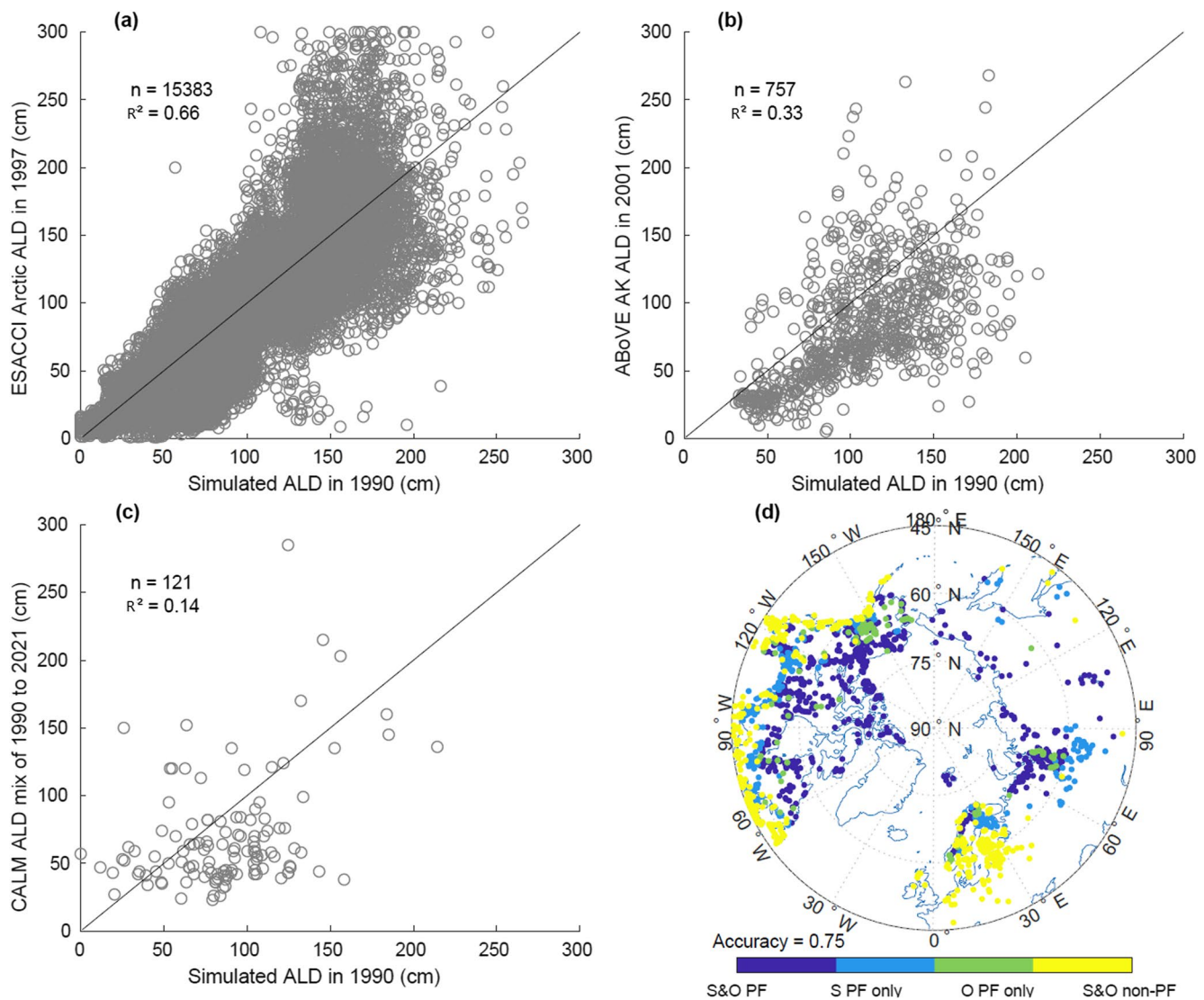


Figure 5. Comparison between simulated active layer depth (ALD) in 1990 and permafrost existence in peat in 1990 with the literature: (a) comparison with satellite-derived Arctic ALD 1997 (Obu et al., 2020); (b) comparison with satellite-derived Alaskan ALD in 2001 (Yi & Kimball, 2020); (c) comparison with ALD from CALM observation network (various years during 1990–2021; Brown et al., 2000; Calm, 1991-); (d) comparison with permafrost in peat record in core data. S&O PF indicates both simulation and observation have permafrost, S PF only indicates permafrost exist in only simulation, O PF only indicates permafrost exist in only observed core records, S&O non-PF indicates no permafrost existence in simulation or observed core data.

In the permafrost region, the deepening ALD from 15 to 7 ka BP indicates that a part of permafrost became warmer during this period (Appendix Figures S7 and S8 in Supporting Information S1). However, this warming trend was mild and did not cause the shrinkage of the permafrost distribution area (Appendix Figures S7 and S9 in Supporting Information S1). With the accumulation of peat, permafrost area started to expand after 9 ka BP, and continued to 7 ka BP (Figure 8). After 7 ka BP, an increasing trend in permafrost area was simulated for part of the pan-Arctic region, which peaked during 500–250a BP (Appendix Figure S9 in Supporting Information S1). The increases in permafrost area during 7–1 ka BP was mild compared with the trend after 1 ka BP (Appendix Figure S9 in Supporting Information S1). Although ALD in the cooling permafrost region became shallower, the cooling was not severe enough to expand permafrost into most of the originally non-permafrost region except for the European southern permafrost boundary during 3–1 ka BP (Appendix Figure S9 in Supporting Information S1). An example based on a representative grid cell is shown by Appendix Figure S10 in Supporting Information S1 supporting this argument. Although decrease in temperature, increase in snowpack, and shallower ALD are simulated, the peat thickness increases faster than ALD shallowing, and thereby becomes the

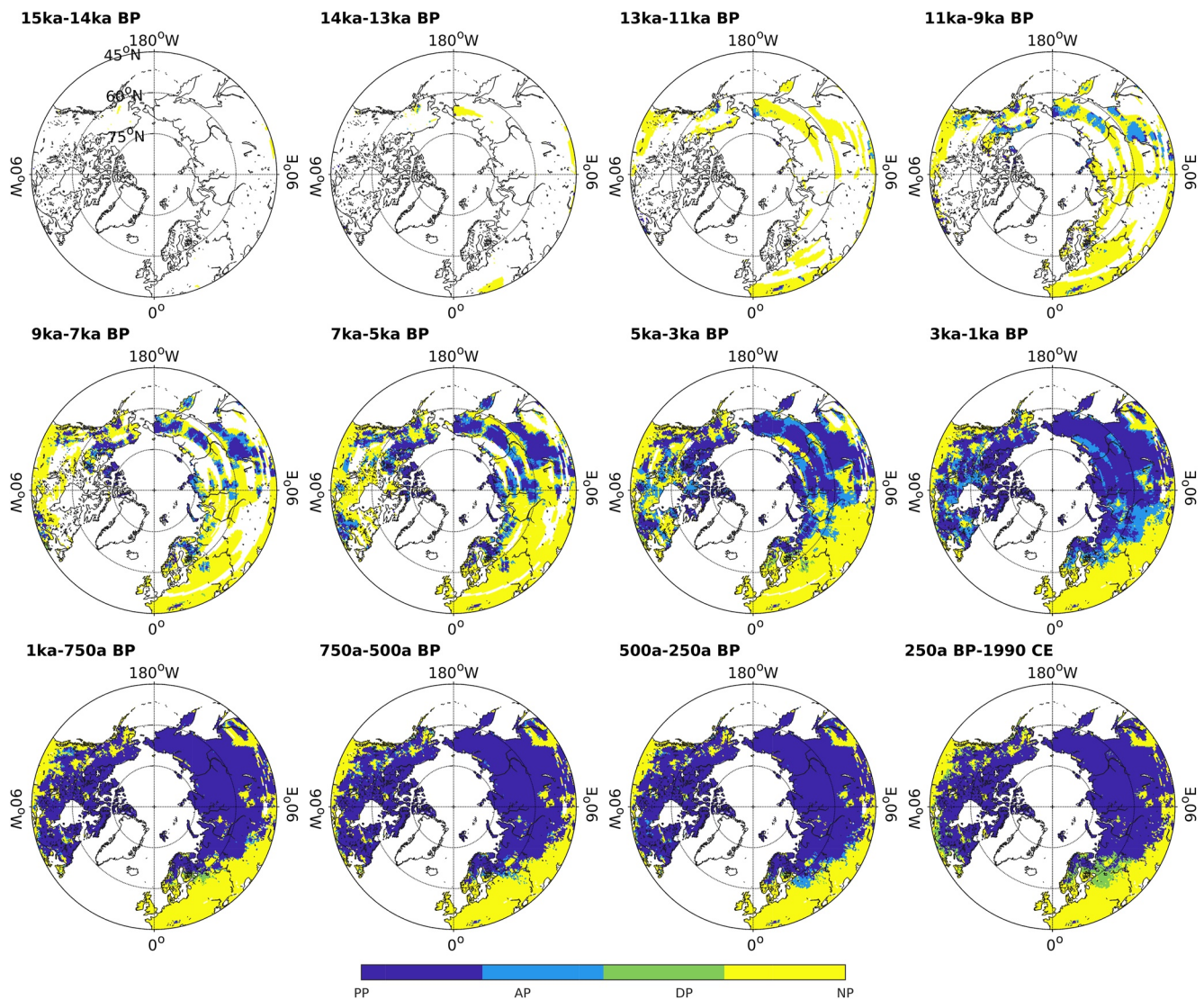


Figure 6. Permafrost dynamics in peatlands from 14 ka BP to 1990 CE. PP represents persistent permafrost, AP represents aggrading permafrost, DP represents degrading permafrost, and NP represents no permafrost.

main driver of permafrost formation (Appendix Figure S10 in Supporting Information S1). Under both cooling permafrost and peat accumulation, permafrost expansion in peat was faster during this period and peaked during 3–1 ka BP (0.86 M km² under average peatland coverage, Figures 6 and 7). Notably, while the northern permafrost became colder during 7–1 ka BP, the southern permafrost mostly became warmer (Appendix Figure S8 in Supporting Information S1). During 1 ka BP–750a BP and 750–500a BP, ALD showed more dynamics than before 1 ka BP. In particular, during 1 ka BP–750a BP, permafrost area increase continued for northern and southern permafrost regions while permafrost degradation dominated the middle permafrost region; during 750–500a BP, ALD in most permafrost regions became deeper except for the northern permafrost regions in Eurasia (Appendix Figure S7 in Supporting Information S1). During 1 ka BP–500a BP, occasional soil and peat permafrost expansion and shrinking were simulated at the southern permafrost boundary (Appendix Figures S6 and S9 in Supporting Information S1).

More severe changes in ALD and permafrost existence were found after 500a BP. During 500–250a BP, a significant permafrost aggradation trend covered most of the permafrost regions (Appendix Figures S7 and S8 in Supporting Information S1), with permafrost distribution expanded at the southern permafrost boundary (Appendix Figures S6 and S9 in Supporting Information S1). After 250a BP, a severe and overwhelming permafrost

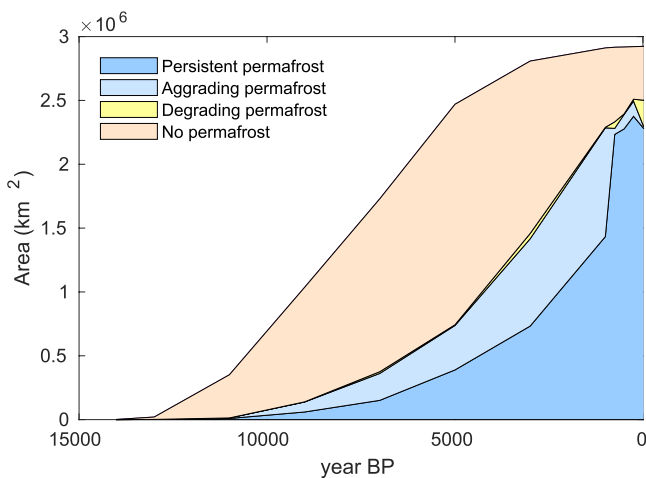


Figure 7. The peatland area of persistent permafrost, aggrading permafrost, degrading permafrost and no permafrost during 15 ka BP–1990. The computed time interval is the same as Figure 7. The peatland coverage is the average peatland coverage of estimates from Hugelius et al. (2020), Melton et al. (2022), and Xu et al. (2018).

degradation trend covered the pan-Arctic region, with more deepening ALD in the southern permafrost (Appendix Figures S7 and S8 in Supporting Information S1). At the southern permafrost boundary, the region that developed permafrost in peat during the cooling in 500–250a BP mostly thawed, together with some regions that developed permafrost before 250a BP (Figure 6).

3.4. Changes in C Fluxes During 500a BP–1990

The study region was categorized into three types of grid cells: ones that developed permafrost during 500–250a BP and thawed by 1990 (“freeze-thaw”), permafrost grid cells and permafrost-free grid cells. Fifty-year means of three-time slices were used, including 500–450a BP, 275–225 a BP, and 1940–1990 to compare their C dynamics under different climate and permafrost conditions (Figure 8). The temperature variation during these three periods is similar under all permafrost conditions. In particular, for the freeze-thaw, permafrost and permafrost-free grid cells, the median temperature in 500–450a BP dropped by 1.1°C, 0.5°C, and 0.7°C in 275–225a BP, respectively, then increased by 0.9°C, 1.5°C, and 1.0°C in 1940–1990, respectively (Figure 8(1)). Therefore, the permafrost region showed the least cooling and the most warming. Meanwhile, from 500–450a BP to 275–225a BP, the median permafrost-free peat thickness in the freeze-thaw and permafrost regions are similar (differ by 1.1 and 1.9 cm, respectively). In contrast,

this value in the permafrost-free region is larger (4.0 cm). From 275–225a BP to 1940–1990, under warmer climate, the median permafrost-free peat thickness in the freeze-thaw, permafrost and permafrost-free regions all increased by 10.0, 10.6, and 6.9 cm, respectively (Figure 8(2)). Notably, the permafrost-free peat thickness is the minimum of ALD and peat thickness. In the permafrost-free and freeze-thaw region, this value is often peat thickness, while in the permafrost region, this value tends to be ALD (Appendix Figure S10 in Supporting Information S1). Median decomposition in the freeze-thaw, permafrost and permafrost-free regions show the same trend that 275–225a BP was the lowest (126.5, 75.6, and 140.1 g C · m⁻² yr⁻¹, respectively), following by 500–450a BP (137.7, 75.8, and 143.1 g C · m⁻² yr⁻¹) and 1940–1990 (156.1, 85.7, and 158.2 g C · m⁻² yr⁻¹; Figure 8(3)). Notably, the trend of both aerobic and anaerobic decomposition are consistent with the total decomposition (Appendix Figure S11 in Supporting Information S1). This indicates that the trend of aerobic and anaerobic decomposition are primarily controlled by the factors that influence them both, which is likely temperature. Meanwhile, the decomposition rate in warmer permafrost-free regions were generally higher than that in the colder freeze-thaw regions and the coldest permafrost regions. During 500–450a BP, the median decomposition in the freeze-thaw and permafrost-free regions differed by 5.4 g C · m⁻² yr⁻¹, while this difference enlarged to 13.6 g C · m⁻² yr⁻¹ as permafrost aggraded in the freeze-thaw region. Therefore, for the freeze-thaw region, the lower decomposition in 275–225a BP was not only caused by lower temperature, but also permafrost aggradation.

For the freeze-thaw and the permafrost-free regions, median NPP mainly kept increasing from 500a BP to 250 BP and from 250 BP to 1990 (by 8.4, 4.6, and –0.1 g C · m⁻² yr⁻¹). However, for the permafrost region, median NPP first slightly declined then increased (89.8 to 88.5 to 101.3 g C · m⁻² yr⁻¹; Figure 8(4)). For the freeze-thaw and the permafrost-free regions, as a result of lower decomposition, the CAR in 275–225a BP was the highest (30.2 and 20.2 g C · m⁻² yr⁻¹), higher than that in 500–450a BP (10.1 and 10.6 g C · m⁻² yr⁻¹) and in 1940–1990 (19.9 and 9.1 g C · m⁻² yr⁻¹). Notably, as a result of the lower decomposition in the freeze-thaw region, the median CAR was 10.0 g C · m⁻² yr⁻¹ higher than the permafrost-free region during 275–225a BP. For the permafrost region, the CAR kept increasing from 500a BP–1990 (12.8–13.0–15.6 g C · m⁻² yr⁻¹; Figure 8(5)).

4. Discussion

4.1. Peatland C Stocks and Fluxes

Our estimated northern peatland soil C stock is 396–421 Pg C depending on the peatland coverage (Table 1). The estimation is biased by the model and parameter uncertainties (Appendix Text S2 in Supporting Information S1). This range agrees with the values in Hugelius et al. (2020), Qiu et al. (2019), and Spahni et al. (2013), is lower

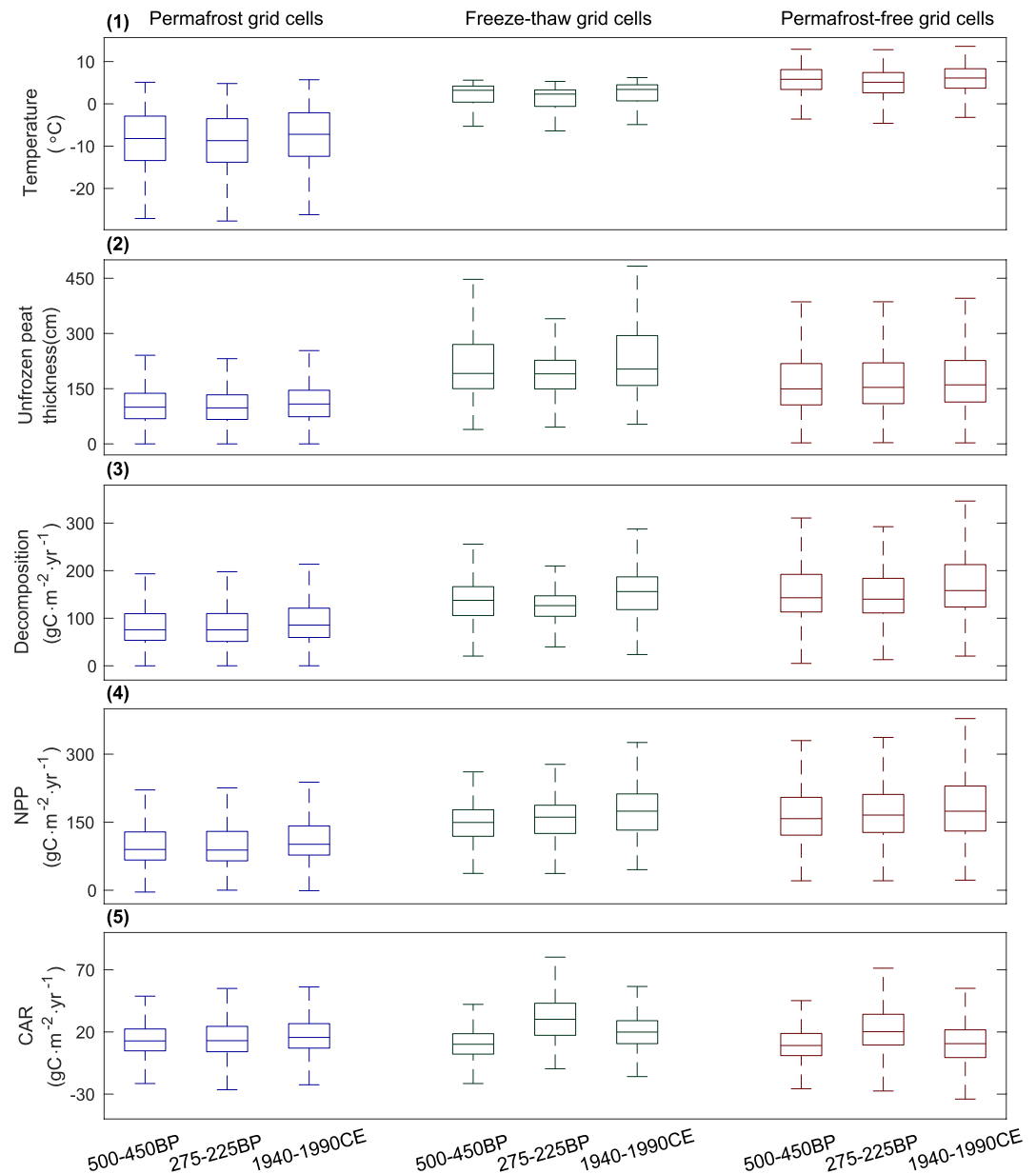


Figure 8. Temperature, unfrozen peat thickness, decomposition, NPP and CAR of the grid cells that left panel: permafrost formed during 500–250a BP and thawed during 250a BP–1990 CE; middle panel: permafrost persisted during 500a BP–1990 CE; right panel: permafrost did not exist during 500a BP–1990 CE. The lines in the boxes are median values of the 50 yr average values, boxes are interquartile range (25%–75%) values, and whiskers are the most extreme values not considered outliers. Outliers are defined as more than 1.5 IQR from the top or bottom line.

than the values reported by Gorham (1991), Loisel et al. (2014), Nichols and Peteet (2019), and Yu et al. (2010), and higher than the values in Hugelius et al. (2013) and Müller and Joos (2021). Notably, the peat expansion trend established from CDF shows a delayed peatland expansion than the trend in Nichols and Peteet (2019), Xu et al. (2018), and Yu et al. (2010). If an earlier peat expansion is used in this study, the total C stock could be larger. The soil C spatial correlation (r value) between this study and Qiu et al. (2019) is 0.38–0.47 depending on peatland coverage map, is 0.49–0.60 between this study and Hugelius et al. (2013), and is 0.69–0.88 between this study and Hugelius et al. (2020) (Appendix Table S3 in Supporting Information S1). There are two reasons that the correlation with Hugelius et al. (2020) is higher than that with the other two data sets. First, the run-on parameters were calculated based on the peat thickness data in Hugelius et al. (2020), and run-on influences WTD and thereby decomposition in PTEM (Zhao, Zhuang, Treat, et al., 2022). Second, the soil C in Hugelius et al. (2020)

was derived by a machine learning approach and the training samples include data from thousands of peat cores. In this study, spatially explicit peat C is sensitive to the C_{\max} value derived from regional calibration, and the data set used in our regional calibration has a substantial overlap with the training samples in Hugelius et al. (2020). In general, both the spatial pattern and regional total of peat C in this study agree with multiple previous studies (Gorham, 1991; Hugelius et al., 2013, 2020; Loisel et al., 2014; Müller & Joos, 2021; Nichols & Peteet, 2019; Qiu et al., 2019; Spahni et al., 2013; Yu et al., 2010).

The spatially explicit CAR from peat initiation 1990CE is presented in Appendix Figure S14 in Supporting Information S1. An obvious discrepancy between our simulated pan-Arctic temporal CAR trend and the core-derived CAR trend in Loisel et al. (2014) is that the simulated 500 yr bin CAR was lower during 1.5 ka BP-present (Figure 3a). However, this discrepancy with Loisel et al. (2014) is also found in Chaudhary et al. (2020) and Nichols and Peteet (2019), both of which are modeling studies covering all northern peatlands. Despite the discrepancy, the core-derived long-term CAR generally agrees with the simulated CAR in the corresponding $0.5^\circ \times 0.5^\circ$ grid cells (Figure 4b). A possible explanation to this discrepancy might be the insufficient core sample availability in the recent millennia. However, the regional long-term CAR values were the same in this study and Loisel et al. (2014) (22.9 vs. 22.9 ± 2 g C·m⁻² yr⁻¹, Table 1). This CAR value is higher than the core-derived value in Yu et al. (2009) and model simulation in Chaudhary et al. (2020) by 4.3 and 1.5 g C·m⁻² yr⁻¹, respectively, but falls within the range of Nichols and Peteet (2019), Treat, Jones, Camill, et al. (2016) and Turunen et al. (2002).

Our estimated median CH₄ production is 2.9–3.4 g C·m⁻² yr⁻¹ for the permafrost region, 12.4–15.5 g C·m⁻² yr⁻¹ for the freeze-thaw region and 17.5–19.4 g C·m⁻² yr⁻¹ for the permafrost-free region (Appendix Figure S12 in Supporting Information S1). These values are all within the 95% confidence interval of CH₄ fluxes for permafrost, permafrost thaw and permafrost-free regions reported by Treat, Jones, Brosius, et al. (2021). Compared with the CH₄ emission reconstructed from cores (Treat, Jones, Brosius, et al., 2021), our estimated CH₄ production started raising latter, but became higher than the core after 5 ka BP (Appendix Figure S13 in Supporting Information S1). However, their trend are in general consistent with each other. In particular, after 1 ka BP, both simulated and core record declined, possibly in response to the onset of LIA.

4.2. Holocene Permafrost Aggradation and Degradation

The simulated ALD in 1990 correlates most closely with a satellite-derived ALD in 1997 (Obu et al., 2020), followed by a satellite-derived ALD in 2001 (Yi & Kimball, 2020) and observed ALD in different years (1990–2021; Brown et al., 2000; Figure 5). The better correlation is found when the temporal gap between two data sets is smaller and when more grid cells are available for comparison, while the different algorithms used to derive ALD from remote sensing imagery may also influence the correlation. As ALD becomes deeper across the Northern Hemisphere (Luo et al., 2016), the difference between ALD in 1990 and 1997 should be less than the difference between 1990 and 2001, and between 1990 and various years during 1990–2021. Possibly due to the recent permafrost thaw, most of the bias between simulated permafrost-in-peat in 1990 and core observation occurs in the southern permafrost region where the data from peat cores show no permafrost (Figure 5d). A previous study has suggested severe ALD deepening and permafrost degradation in the southern permafrost region during 1982–2015 (Peng et al., 2020). As the cores were mostly collected after 1990 (Hugelius et al., 2020; Treat, Jones, Camill, et al., 2016), it is possible that some cores in this region having deep ALD in 1990 were thawed by the time of core collection.

Our simulation indicates that ALD is getting shallower as peat accumulates (Appendix Figure S10 in Supporting Information S1), which is consistent with the observed shallower ALD at peatland sites and the modeling study shows there is lower soil temperature with more organic matter (Brown et al., 2000; Lawrence & Slater, 2008). In addition to peat accumulation, another driver to ALD dynamics is the temperature. Consistent with the paleo-temperature database, TraCE data set shows that Holocene global mean surface temperature reached its peak around 6.5 ka BP during the Holocene Thermal Maximum (HTM) (Kaufman et al., 2020; Appendix Figure S15 in Supporting Information S1), the simulated ALD generally became deeper until 7 ka BP. During 7–6 ka BP, a multiproxy paleo-climate data set indicates that Neoglacial cooling started in the Northern Hemisphere, with different start time in different regions (McKay et al., 2018). This cooling trend is not shown by the ALD dynamics during 7–5 ka BP simulated in this study, possibly because the ALD change rate is slower than our selected threshold (Appendix Figure S8 in Supporting Information S1). Meanwhile, the peat core data indicate

permafrost development in Alaska, Siberia, and Arctic Canada before 4 ka BP (Treat & Jones, 2018), which is consistent with the permafrost in peat distribution in 7 and 5 ka BP (Figure 6). During Neoglacial cooling, we simulated a widespread permafrost expansion which peaked during 3–1 ka BP. Both our simulation and core data suggest permafrost distribution increased in Arctic Canada, eastern Northern America, and Arctic and European Russia after 3 ka BP (Treat & Jones, 2018). After 1 ka BP, the simulation showed deepening ALD in most of the permafrost regions during 1 ka BP–500a BP, which was approximately the Medieval Climate Anomaly (MCA) when most of Eurasia Arctic and parts of North America warmed (Mann et al., 2009). During 500–250a BP, ALD generally became shallower in permafrost region (Appendix Figure S8 in Supporting Information S1), with permafrost expansion found in west Eurasia. This period is approximately the Little Ice Age (LIA), when cooling dominated the Northern Hemisphere (Mann et al., 2009). The deepening of ALD and permafrost coverage shrink in west Eurasia after 250a BP reflects the increase of greenhouse gas emissions, radiative forcing and temperature since 1750 (IPCC, 2007). In general, the temporal trend of the simulated ALD and permafrost in peat agrees with the paleo-climate data set and core information.

4.3. Influence of Climate Change on Peat Carbon Accumulation Rate

During 500–250a BP, the onset of the LIA triggered permafrost aggradation and the decrease in decomposition in west Eurasia. This could partially explain the reason that median CAR of the freeze-thaw region is higher than the permafrost-free region by $10.0 \text{ g C} \cdot \text{m}^{-2} \text{ yr}^{-1}$. The freeze-thaw and the permafrost-free region had the highest CAR during LIA. This is consistent with the findings by analyzing of the peat cores in the discontinuous and sporadic permafrost region, indicating the CAR was the highest during LIA (Zhang et al., 2018). However, during 500a BP–1990, the permafrost region CAR was the highest during 1940–1990 and the same trend is found in western Canada that rapid surficial C accumulation makes up for the deep soil C loss (Heffernan et al., 2020). Under Anthropocene warming, with a similar increase in NPP in three regions ($8.5\text{--}13.2 \text{ g C} \cdot \text{m}^{-2} \text{ yr}^{-1}$), the different responses of CAR result from the different increases in decomposition rates. Previous studies suggest that both CH_4 and CO_2 emissions increase approximately exponentially with temperature below 25°C (Curiel Yuste et al., 2007; Lupascu et al., 2012). Therefore, under the relatively cold climate in the pan-Arctic, the similar temperature increase has different effects in the warmer southern region and colder northern regions. In particular, in the colder permafrost region, median decomposition rates increased by $10.1 \text{ g C} \cdot \text{m}^{-2} \text{ yr}^{-1}$, lower than the median NPP increase, but increased by $18.1\text{--}29.6 \text{ g C} \cdot \text{m}^{-2} \text{ yr}^{-1}$ in the warmer freeze-thaw and permafrost-free region. Therefore, Anthropocene warming enhances C accumulation in the permafrost peat, but weakens the C sink in the newly thawed and permafrost-free peat.

Our study agrees with previous modeling, indicating that northern peatlands are still a C sink, and regional NPP has increased more than decomposition under Anthropocene warming (Qiu et al., 2019). Furthermore, peatlands will still be a C sink until at least 2100 under various RCP conditions (McGuire et al., 2018; Qiu et al., 2020). These modeling studies indicate that despite decomposition increasing more rapidly than NPP under warming conditions, the warming during 1750–2100 does not make decomposition high enough to override NPP. However, temperature is very likely to keep increasing after 2100 (Palmer et al., 2018), resulting in further permafrost warming (Peng et al., 2020) and permafrost degradation in various regions (Czerniawska & Chlachula, 2020; Plaza et al., 2019). As a result, part of the current permafrost region will likely switch to newly thawed or permafrost-free conditions, where decomposition increases faster than NPP does under the same warming. This trend is already shown in relatively warm northern peatlands. In particular, the lower latitude northern peatlands generally show a trend of lower CAR during higher temperature and vice versa (Appendix Figure S18 in Supporting Information S1). More importantly, the southernmost peatlands have already switched from C sinks to C sources during Anthropocene warming (Appendix Figure S19 in Supporting Information S1).

4.4. Future Work

PTEM 2.1 is able to simulate C dynamics for the Holocene. Our next step would be applying it to future simulations to project northern peatlands responses to future climate change. In particular, the Holocene simulation provides spatially explicit peat profile, which is informative for initializing future northern peatland simulation. However, there are issues to be addressed in the model. First, although PTEM 2.1 is able to simulate run-on and run-off, the estimation of run-on and run-off highly relies on the existing model products, which introduces uncertainties (Fan et al., 2013). In addition, the estimation for run-on is based on a constant spatially explicit

theoretical maximum run-on value. This method is reasonable only under the relatively stable climate condition, but likely will result in high biases in future simulations. Second, although comparison with literature indicates our estimation of k_d and C_{\max} values are reasonable for instance, the parameterization process can be further improved if flux tower measurements and site-level observations from various locations become more available in the future.

5. Conclusions

Our machine learning approach reasonably estimated peat basal ages of northern peatlands. Our simulated regional peatland C stock and long-term carbon accumulation rate are consistent with the literature. We estimate that regional peatland C stocks are 396–421 Pg C depending on peatland coverage, and that the regional mean Holocene carbon accumulation rate has been $22.9 \text{ g C} \cdot \text{m}^{-2} \text{ yr}^{-1}$. The PTEM 2.2 simulated active layer depth agrees with multiple data sets, and thereby we reconstruct the permafrost development in peat from 15 ka BP to 1990. Peat permafrost development generally started around 7 ka BP, peaked during 3–1 ka BP, and has stabilized since 1 ka BP. The temporal dynamics of active layer depth and permafrost dynamics are generally consistent with the timing of the Holocene Thermal Maximum (~11 ka–5 ka BP), Neoglacial cooling (~7 ka–2 ka BP, various in different regions), the MCA (~1 ka–750a BP), the LIA (~550a–250a BP) and Anthropocene warming (since ~200a BP).

From the Medieval Climate Anomaly to Anthropocene warming, we have classified northern peatlands into three categories depending on the permafrost condition: the region that developed permafrost in the LIA and thawed in the Anthropocene, the persistent permafrost region, and the permafrost-free region. We found that peatland C fluxes respond to climate warming differently in these three regions. As the freeze-thaw and permafrost-free regions are warmer, Anthropocene climate warming enhances decomposition more than NPP and thereby the C sink capacity decreases or is lost. On the contrary, the colder permafrost region showed higher carbon accumulation rates under Anthropocene warming due to NPP increasing more than decomposition. Therefore, under future climate warming, the current permafrost region will likely switch to less permafrost or permafrost-free conditions, and the C sink capacity of peatlands will decrease.

Data Availability Statement

The data in this study can be accessed from Purdue University Research Repository: Zhao, Zhuang, and Frolking (2022). Modeling carbon accumulation and greenhouse gas emissions of northern peatlands since the Holocene. Purdue University Research Repository. doi:10.4231/6647-C769. <https://purr.purdue.edu/publications/4054/2>.

References

- Allen, M. R., Dube, O. P., Solecki, W., Aragón-Durand, F., Cramer, W., Kainuma, M., et al. (2018). Framing and context. In *Global warming of 1.5°C. An IPCC special report on the impacts of global warming of 1.5°C above pre-industrial levels and related global greenhouse gas emission pathways, in the context of strengthening the global response to the threat of climate change, sustainable development, and efforts to eradicate poverty*.
- Brown, J., Hinkel, K. M., & Nelson, F. E. (2000). The circumpolar active layer monitoring (CALM) program: Research designs and initial results. *Polar Geography*, 24(3), 166–258. <https://doi.org/10.1080/10889370009377698>
- Chaudhary, N., Miller, P. A., & Smith, B. (2017). Modeling past, present and future peatland carbon accumulation across the pan-Arctic region. *Biogeosciences*, 14(18), 4023–4044. <https://doi.org/10.5194/bg-14-4023-2017>
- Chaudhary, N., Westermann, S., Lamba, S., Shurpali, N., Sannel, A. B. K., Schurgers, G., et al. (2020). Modeling past and future peatland carbon dynamics across the pan-Arctic. *Global Change Biology*, 26(7), 4119–4133. <https://doi.org/10.1111/gcb.15099>
- Cheremisnoff, N. P. (Ed.). (1997). Groundwater remediation and treatment technologies (p. vi). Westwood, NJ: William Andrew Publishing.
- CRU (University of East Anglia Climatic Research Unit). (2018). CRU TS4.03: Climatic research unit (CRU) time-series (TS) version 4.03 of high-resolution gridded data of month-by-month variation in climate.
- Curriel Yuste, J., Baldocchi, D. D., Gershenson, A., Goldstein, A., Misson, L., & Wong, S. (2007). Microbial soil respiration and its dependency on carbon inputs, soil temperature, and moisture. *Global Change Biology*, 13(9), 2018–2035. <https://doi.org/10.1111/j.1365-2486.2007.01415.x>
- Czerniawska, J., & Chlachula, J. (2020). Climate-change induced permafrost degradation in Yakutia, East Siberia. *ARCTIC*, 73(4), 509–528. <https://doi.org/10.14430/arctic71674>
- Doherty, J., Hayes, D., & Muffels, C. (2022). Pest, model independent parameter estimation and uncertainty analysis.
- Fan, Y., Li, H., & Miguez-Macho, G. (2013). Global patterns of groundwater table depth. *Science*, 339(6122), 940–943. <https://doi.org/10.1126/science.1229881>
- FAO/UNESCO. (1974). *Soil map of the world*. Paris.

Acknowledgments

The authors thank Joe Melton for providing data and commenting on an earlier version of this paper. The research is supported by NSF projects # 1802832 and 1802825.

- Frolking, S., Roulet, N. T., Tuittila, E., Bubier, J. L., Quillet, A., Talbot, J., & Richard, P. J. H. (2010). A new model of Holocene peatland net primary production, decomposition, water balance, and peat accumulation. *Earth System Dynamics*, *1*(1), 1–21. <https://doi.org/10.5194/esd-1-1-2010>
- Frolking, S., Talbot, J., Jones, M. C., Treat, C. C., Kauffman, J. B., Tuittila, E.-S., & Roulet, N. (2011). Peatlands in the Earth's 21st century climate system. *Environmental Reviews*, *19*, 371–396. Retrieved from <https://cdnsiencepub.com/doi/abs/10.1139/a11-014>
- Gallego-Sala, A. V., Charman, D. J., Brewer, S., Page, S. E., Prentice, I. C., Friedlingstein, P., et al. (2018). Latitudinal limits to the predicted increase of the peatland carbon sink with warming. *Nature Climate Change*, *8*(10), 907–913. <https://doi.org/10.1038/s41558-018-0271-1>
- GISTEMP-Team. (2021). GISS surface temperature analysis (GISTEMP), version 4, NASA goddard institute for space studies.
- Gorham, E. (1991). Northern peatlands: Role in the carbon cycle and probable responses to climatic warming. *Ecological Applications*, *1*(2), 182–195. <https://doi.org/10.2307/1941811>
- Gorham, E., Lehman, C., Dyke, A., Janssens, J., & Dyke, L. (2007). Temporal and spatial aspects of peatland initiation following deglaciation in North America. *Quaternary Science Reviews*, *26*(3), 300–311. <https://doi.org/10.1016/j.quascirev.2006.08.008>
- Granberg, G., Grip, H., Löfvenius, M. O., Sundh, I., Svensson, B. H., & Nilsson, M. (1999). A simple model for simulation of water content, soil frost, and soil temperatures in boreal mixed mires. *Water Resources Research*, *35*(12), 3771–3782. <https://doi.org/10.1029/1999WR900216>
- He, F. (2011). *Simulating transient climate evolution of the last deglaciation with CCSM3 (Doctor of Philosophy)*. Madison: University of Wisconsin-Madison.
- Heffernan, L., Estop-Aragónés, C., Knorr, K.-H., Talbot, J., & Olefeldt, D. (2020). Long-term impacts of permafrost thaw on carbon storage in peatlands: Deep losses offset by surficial accumulation. *Journal of Geophysical Research: Biogeosciences*, *125*(3), e2019JG005501. <https://doi.org/10.1029/2019JG005501>
- Huang, Y., Ciais, P., Luo, Y., Zhu, D., Wang, Y., Qiu, C., et al. (2021). Tradeoff of CO₂ and CH₄ emissions from global peatlands under water-table drawdown. *Nature Climate Change*, *11*(7), 618–622. <https://doi.org/10.1038/s41558-021-01059-w>
- Hugelius, G., Bockheim, J. G., Camill, P., Elberling, B., Grosse, G., Harden, J. W., et al. (2013). A new data set for estimating organic carbon storage to 3 m depth in soils of the northern circumpolar permafrost region. *Earth System Science Data*, *5*(2), 393–402. <https://doi.org/10.5194/essd-5-393-2013>
- Hugelius, G., Loisel, J., Chadburn, S., Jackson, R. B., Jones, M., MacDonald, G., et al. (2020). Large stocks of peatland carbon and nitrogen are vulnerable to permafrost thaw. *Proceedings of the National Academy of Sciences*, *117*(34), 20438–20446. <https://doi.org/10.1073/pnas.1916387117>
- IPCC. (2007). *Climate change 2007: The physical science basis. Contribution of Working Group I to the Fourth Assessment Report of the Intergovernmental Panel on Climate Change*. Cambridge, United Kingdom and New York, NY, USA.
- Jones, M. C., Harden, J., O'Donnell, J., Manies, K., Jorgenson, T., Treat, C., & Ewing, S. (2017). Rapid carbon loss and slow recovery following permafrost thaw in boreal peatlands. *Global Change Biology*, *23*(3), 1109–1127. <https://doi.org/10.1111/gcb.13403>
- Kaufman, D., McKay, N., Routson, C., Erb, M., Dätwyler, C., Sommer, P. S., et al. (2020). Holocene global mean surface temperature, a multi-method reconstruction approach. *Scientific Data*, *7*(1), 201. <https://doi.org/10.1038/s41597-020-0530-7>
- Korhola, A., Ruppel, M., Seppä, H., Väliranta, M., Virtanen, T., & Weckström, J. (2010). The importance of northern peatland expansion to the late-Holocene rise of atmospheric methane. *Quaternary Science Reviews*, *29*(5), 611–617. <https://doi.org/10.1016/j.quascirev.2009.12.010>
- Lawrence, D. M., & Slater, A. G. (2008). Incorporating organic soil into a global climate model. *Climate Dynamics*, *30*(2), 145–160. <https://doi.org/10.1007/s00382-007-0278-1>
- Loisel, J., Van Bellen, S., Pelletier, L., Talbot, J., Hugelius, G., Karran, D., et al. (2017). Insights and issues with estimating northern peatland carbon stocks and fluxes since the last glacial maximum. *Earth-Science Reviews*, *165*, 59–80. <https://doi.org/10.1016/j.earscirev.2016.12.001>
- Loisel, J., Yu, Z., Beilman, D. W., Camill, P., Alm, J., Amesbury, M. J., et al. (2014). A database and synthesis of northern peatland soil properties and Holocene carbon and nitrogen accumulation. *The Holocene*, *24*(9), 1028–1042. <https://doi.org/10.1177/0959683614538073>
- López-Blanco, E., Jackowicz-Korczynski, M., Mastepanov, M., Skov, K., Westergaard-Nielsen, A., Williams, M., & Christensen, T. R. (2020). Multi-year data-model evaluation reveals the importance of nutrient availability over climate in Arctic ecosystem C dynamics. *Environmental Research Letters*, *15*(9), 094007. <https://doi.org/10.1088/1748-9326/ab865b>
- Luo, D., Wu, Q., Jin, H., Marchenko, S. S., Lü, L., & Gao, S. (2016). Recent changes in the active layer thickness across the Northern Hemisphere. *Environmental Earth Sciences*, *75*(7), 555. <https://doi.org/10.1007/s12665-015-5229-2>
- Lupascu, M., Wadham, J. L., Hornibrook, E. R. C., & Pancost, R. D. (2012). Temperature sensitivity of methane production in the permafrost active layer at Stordalen, Sweden: A comparison with non-permafrost northern wetlands. *Arctic Antarctic and Alpine Research*, *44*(4), 469–482. <https://doi.org/10.1657/1938-4246-44.4.469>
- MacDonald, G. M., Beilman, D. W., Kremenetski, K. V., Sheng, Y., Smith, L. C., & Velichko, A. A. (2006). Rapid early development of circumarctic peatlands and atmospheric CH₄ and CO₂ variations. *Science*, *314*(5797), 285–288. <https://doi.org/10.1126/science.1131722>
- Mann, M. E., Zhang, Z., Rutherford, S., Bradley Raymond, S., Hughes Malcolm, K., Shindell, D., et al. (2009). Global signatures and dynamical origins of the little ice age and medieval climate anomaly. *Science*, *326*(5957), 1256–1260. <https://doi.org/10.1126/science.1177303>
- McCalley, C. K., Woodcroft, B. J., Hodgkins, S. B., Wehr, R. A., Kim, E.-H., Mondav, R., et al. (2014). Methane dynamics regulated by microbial community response to permafrost thaw. *Nature*, *514*(7523), 478–481. <https://doi.org/10.1038/nature13798>
- McGuire, A. D., Lawrence, D. M., Koven, C., Clein, J. S., Burke, E., Chen, G., et al. (2018). Dependence of the evolution of carbon dynamics in the northern permafrost region on the trajectory of climate change. *Proceedings of the National Academy of Sciences*, *115*(15), 3882–3887. <https://doi.org/10.1073/pnas.1719903115>
- McKay, N. P., Kaufman, D. S., Routson, C. C., Erb, M. P., & Zander, P. D. (2018). The onset and rate of Holocene neoglaciation in the Arctic. *Geophysical Research Letters*, *45*(22), 12487–12496. <https://doi.org/10.1029/2018GL079773>
- Melton, J. R., Chan, E., Millard, K., Fortier, M., Winton, R. S., Martín-López, J. M., et al. (2022). A map of global peatland extent created using machine learning (Peat-ML). *Geoscientific Model Development Discussions*, *2022*, 1–44. <https://doi.org/10.5194/gmd-2021-426>
- Müller, J., & Joos, F. (2021). Committed and projected future changes in global peatlands—Continued transient model simulations since the last glacial maximum. *Biogeosciences*, *18*(12), 3657–3687. <https://doi.org/10.5194/bg-18-3657-2021>
- Nichols, J. E., & Peteet, D. M. (2019). Rapid expansion of northern peatlands and doubled estimate of carbon storage. *Nature Geoscience*, *12*(11), 917–921. <https://doi.org/10.1038/s41561-019-0454-z>
- Obu, J., Westermann, S., Barboux, C., Bartsch, A., Delaloye, R., Grosse, G., et al. (2020). ESA permafrost climate change initiative (permafrost_cci): Permafrost climate research data package v1.
- O'Donnell, J. A., Jorgenson, M. T., Harden, J. W., McGuire, A. D., Kanevskiy, M. Z., & Wickland, K. P. (2012). The effects of permafrost thaw on soil hydrologic, thermal, and carbon dynamics in an Alaskan peatland. *Ecosystems*, *15*(2), 213–229. <https://doi.org/10.1007/s10021-011-9504-0>

- Palmer, M. D., Harris, G. R., & Gregory, J. M. (2018). Extending CMIP5 projections of global mean temperature change and sea level rise due to thermal expansion using a physically based emulator. *Environmental Research Letters*, 13(8), 084003. <https://doi.org/10.1088/1748-9326/aad2e4>
- Pedregosa, F., Varoquaux, G., Gramfort, A., Michel, V., Thirion, B., Grisel, O., et al. (2011). Scikit-learn: Machine learning in python. *Journal of Machine Learning Research*, 12, 2825–2830.
- Peng, X., Zhang, T., Frauenfeld, O. W., Wang, S., Qiao, L., Du, R., & Mu, C. (2020). Northern Hemisphere greening in association with warming permafrost. *Journal of Geophysical Research: Biogeosciences*, 125(1), e2019JG005086. <https://doi.org/10.1029/2019JG005086>
- Plaza, C., Pegoraro, E., Bracho, R., Celis, G., Crummer, K. G., Hutchings, J. A., et al. (2019). Direct observation of permafrost degradation and rapid soil carbon loss in tundra. *Nature Geoscience*, 12(8), 627–631. <https://doi.org/10.1038/s41561-019-0387-6>
- Qiu, C., Ciais, P., Zhu, D., Guenet, B., Peng, S., Petrescu, A. M. R., et al. (2021). Large historical carbon emissions from cultivated northern peatlands. *Science Advances*, 7(23), eabf1332. <https://doi.org/10.1126/sciadv.abf1332>
- Qiu, C., Zhu, D., Ciais, P., Guenet, B., & Peng, S. (2020). The role of northern peatlands in the global carbon cycle for the 21st century. *Global Ecology and Biogeography*, 29(5), 956–973. <https://doi.org/10.1111/geb.13081>
- Qiu, C., Zhu, D., Ciais, P., Guenet, B., Peng, S., Krinner, G., et al. (2019). Modeling northern peatland area and carbon dynamics since the Holocene with the ORCHIDEE-PEAT land surface model (SVN r5488). *Geoscientific Model Development*, 12(7), 2961–2982. <https://doi.org/10.5194/gmd-12-2961-2019>
- Spahni, R., Joos, F., Stocker, B. D., Steinacher, M., & Yu, Z. C. (2013). Transient simulations of the carbon and nitrogen dynamics in northern peatlands: From the last glacial maximum to the 21st century. *Climate of the Past*, 9(3), 1287–1308. <https://doi.org/10.5194/cp-9-1287-2013>
- Stocker, B. D., Spahni, R., & Joos, F. (2014). DYPOTOP: A cost-efficient TOPMODEL implementation to simulate sub-grid spatio-temporal dynamics of global wetlands and peatlands. *Geoscientific Model Development*, 7(6), 3089–3110. <https://doi.org/10.5194/gmd-7-3089-2014>
- Treat, C. C., & Jones, M. C. (2018). Near-surface permafrost aggradation in Northern Hemisphere peatlands shows regional and global trends during the past 6,000 yr. *The Holocene*, 28(6), 998–1010. <https://doi.org/10.1177/0959683617752858>
- Treat, C. C., Jones, M. C., Alder, J., Sannel, A. B. K., Camill, P., & Frolking, S. (2021). Predicted vulnerability of carbon in permafrost peatlands with future climate change and permafrost thaw in western Canada. *Journal of Geophysical Research: Biogeosciences*, 126(5), e2020JG005872. <https://doi.org/10.1029/2020JG005872>
- Treat, C. C., Jones, M. C., Brosius, L., Grosse, G., Walter Anthony, K., & Frolking, S. (2021). The role of wetland expansion and successional processes in methane emissions from northern wetlands during the Holocene. *Quaternary Science Reviews*, 257, 106864. <https://doi.org/10.1016/j.quascirev.2021.106864>
- Treat, C. C., Jones, M. C., Brosius, L. S., Grosse, G., & Walter Anthony, K. M. (2016). Radiocarbon dates of peatland initiation across the northern high latitudes. <https://doi.org/10.1594/PANGAEA.864101>
- Treat, C. C., Jones, M. C., Camill, P., Gallego-Sala, A., Garneau, M., Harden, J. W., et al. (2016). Effects of permafrost aggradation on peat properties as determined from a pan-Arctic synthesis of plant macrofossils. *Journal of Geophysical Research: Biogeosciences*, 121(1), 78–94. <https://doi.org/10.1002/2015JG003061>
- Turetsky, M. R., Benscoter, B., Page, S., Rein, G., Van Der Werf, G. R., & Watts, A. (2015). Global vulnerability of peatlands to fire and carbon loss. *Nature Geoscience*, 8(1), 11–14. <https://doi.org/10.1038/ngeo2325>
- Turetsky, M. R., Wieder, R. K., & Vitt, D. H. (2002). Boreal peatland C fluxes under varying permafrost regimes. *Soil Biology and Biochemistry*, 34(7), 907–912. [https://doi.org/10.1016/S0038-0717\(02\)00022-6](https://doi.org/10.1016/S0038-0717(02)00022-6)
- Turunen, J., Tomppo, E., Tolonen, K., & Reinikainen, A. (2002). Estimating carbon accumulation rates of undrained mires in Finland-application to boreal and sub-Arctic regions. *The Holocene*, 12(1), 69–80. <https://doi.org/10.1191/0959683602h522rp>
- USGSNGA. (2010). Global multi-resolution terrain elevation data 2010 (GMTED2010).
- Weiss, R., Shurpali, N., Sallantausta, T., Laiho, R., Laine, J., & Alm, J. (2006). Simulation of water table level and peat temperatures in boreal peatlands. *Ecological Modelling*, 192(3–4), 441–456. <https://doi.org/10.1016/j.ecolmodel.2005.07.016>
- Xu, J., Morris, P. J., Liu, J., & Holden, J. (2018). PEATMAP: Refining estimates of global peatland distribution based on a meta-analysis. *CATENA*, 160, 134–140. <https://doi.org/10.1016/j.catena.2017.09.010>
- Yi, Y., & Kimball, J. S. (2020). *Above: Active layer thickness from remote sensing permafrost model, Alaska, 2001–2015*. ORNL Distributed Active Archive Center.
- Yu, Z., Beilman, D., & Jones, M. (2009). Sensitivity of northern peatland carbon dynamics to Holocene climate change. *Washington DC American Geophysical Union Geophysical Monograph Series* (Vol. 184, pp. 55–69). <https://doi.org/10.1029/2008GM000822>
- Yu, Z., Loisel, J., Brosseau, D. P., Beilman, D. W., & Hunt, S. J. (2010). Global peatland dynamics since the last glacial maximum. *Geophysical Research Letters*, 37(13). <https://doi.org/10.1029/2010gl043584>
- Zhang, H., Gallego-Sala, A. V., Amesbury, M. J., Charman, D. J., Piilo, S. R., & Väliranta, M. M. (2018). Inconsistent response of Arctic permafrost peatland carbon accumulation to warm climate phases. *Global Biogeochemical Cycles*, 32(10), 1605–1620. <https://doi.org/10.1029/2018GB005980>
- Zhao, B., Zhuang, Q., & Frolking, S. (2022). *Modeling carbon accumulation and greenhouse gas emissions of northern peatlands since the Holocene*. Purdue University Research Repository. <https://doi.org/10.4231/6647-C769>
- Zhao, B., Zhuang, Q., Treat, C., & Frolking, S. (2022). A model intercomparison analysis for controls on C accumulation in North American peatlands. *Journal of Geophysical Research: Biogeosciences*, 127(5), e2021JG006762. <https://doi.org/10.1029/2021JG006762>
- Zhuang, Q., McGuire, A. D., O'Neill, K. P., Harden, J. W., Romanovsky, V. E., & Yarie, J. (2002). Modeling soil thermal and carbon dynamics of a fire chronosequence in interior Alaska. *Journal of Geophysical Research: Atmospheres*, 107(D1), FFR3-1–FFR3-26. <https://doi.org/10.1029/2001JD001244>
- Zhuang, Q., Melillo, J. M., Kicklighter, D. W., Prinn, R. G., McGuire, A. D., Steudler, P. A., et al. (2004). Methane fluxes between terrestrial ecosystems and the atmosphere at northern high latitudes during the past century: A retrospective analysis with a process-based biogeochemistry model. *Global Biogeochemical Cycles*, 18(3). <https://doi.org/10.1029/2004GB002239>
- Zhuang, Q., Romanovsky, V., & McGuire, A. (2001). Incorporation of a permafrost model into a large-scale ecosystem model: Evaluation of temporal and spatial scaling issues in simulating soil thermal dynamics. *Journal of Geophysical Research*, 106(D24), 33649–33670. <https://doi.org/10.1029/2001JD900151>
- Zhuang, Q., Wang, S., Zhao, B., Aires, F., Prigent, C., Yu, Z., et al. (2020). Modeling Holocene peatland carbon accumulation in North America. *Journal of Geophysical Research: Biogeosciences*, 125(11), e2019JG005230. <https://doi.org/10.1029/2019JG005230>

References From the Supporting Information

- Clymo, R. S., Kramer, J. R., & Hammerton, D. (1984). Sphagnum-dominated peat bog: A naturally acid ecosystem [and discussion]. *Philosophical Transactions of the Royal Society of London. Series B, Biological Sciences*, 305(1124), 487–499. <http://www.jstor.org/stable/2396100>
- Gao, J., Feng, J., Zhang, X., Yu, F.-H., Xu, X., & Kuzyakov, Y. (2016). Drying-rewetting cycles alter carbon and nitrogen mineralization in litter-amended alpine wetland soil. *CATENA*, 145, 285–290. <https://doi.org/10.1016/j.catena.2016.06.026>
- Glaser, P. H., Siegel, D. I., Chanton, J. P., Reeve, A. S., Rosenberry, D. O., Corbett, J. E., et al. (2016). Climatic drivers for multi-decadal shifts in solute transport and methane production zones within a large peat basin. *Global Biogeochemical Cycles*, 30(11), 1578–1598. <https://doi.org/10.1002/2016GB005397>
- Griffiths, N. A., Sebestyen, S. D., & Oleheiser, K. C. (2019). Variation in peatland porewater chemistry over time and space along a bog to fen gradient. *Science of the Total Environment*, 697, 134152. <https://doi.org/10.1016/j.scitotenv.2019.134152>
- Koerselman, W., Van Kerkhoven, M. B., & Verhoeven, J. T. (1993). Release of inorganic n , p , and k in peat soils; effect of temperature, water chemistry, and water level. *Biogeochemistry*, 20(2), 63–81. <https://doi.org/10.1007/BF00004135>
- Limpens, J., Heijmans, M. M. P. D., & Berendse, F. (2006). The nitrogen cycle in boreal peatlands. In R. K. Wieder, & D. H. Vitt (Eds.), *Boreal peatland ecosystems* (pp. 195–230). Berlin, Heidelberg: Springer Berlin Heidelberg.
- López-Blanco, E., Lund, M., Williams, M., Tamstorf, M. P., Westergaard-Nielsen, A., Exbrayat, J. F., et al. (2017). Exchange of CO₂ in Arctic tundra: Impacts of meteorological variations and biological disturbance. *Biogeosciences*, 14(19), 4467–4483. <https://doi.org/10.5194/bg-14-4467-2017>
- Ojanen, P., Penttilä, T., Tolvanen, A., Hotanen, J.-P., Saarimaa, M., Nousiainen, H., & Minkkinen, K. (2019). Long-term effect of fertilization on the greenhouse gas exchange of low-productive peatland forests. *Forest Ecology and Management*, 432, 786–798. <https://doi.org/10.1016/j.foreco.2018.10.015>
- Olefeldt, D., Hovemyr, M., Kuhn, M. A., Bastviken, D., Bohn, T. J., Connolly, J., et al. (2021). The boreal-Arctic Wetland and Lake Data Set (BAWLD). *Earth System Science Data*, 13(11), 5127–5149. <https://doi.org/10.5194/essd-13-5127-2021>
- Song, Y., Song, C., Ren, J., Tan, W., Jin, S., & Jiang, L. (2018). Influence of nitrogen additions on litter decomposition, nutrient dynamics, and enzymatic activity of two plant species in a peatland in northeast China. *Science of the Total Environment*, 625, 640–646. <https://doi.org/10.1016/j.scitotenv.2017.12.311>
- Treat, C. C., Jones, M. C., Camill, P., Gallego-Sala, A., Garneau, M., Harden, J. W., et al. (2016). Synthesis data set of physical and ecosystem properties from pan-Arctic wetland sites using peat core analysis.
- Vitt, D. H. (2013). Peatlands. In B. Fath (Ed.), *Encyclopedia of ecology* (2nd ed., pp. 557–566). Oxford: Elsevier.
- Wang, S., Zhuang, Q., Yu, Z., Bridgman, S., & Keller, J. K. (2016). Quantifying peat carbon accumulation in Alaska using a process-based biogeochemistry model. *Journal of Geophysical Research: Biogeosciences*, 121(8), 2172–2185. <https://doi.org/10.1002/2016JG003452>